Πανεπιστήμιο Δυτικής Αττικής

Σχολή Μηχανικών

Τμήμα Μηχανολόγων Μηχανικών

Διπλωματική Εργασία

_____

Υδροδυναμική Ανάλυση Ναυτικής Έλικας σε Συνθήκες Ελεύθερης Ροής με Χρήση του Υπολογιστικού Κώδικα OpenFOAM

Αναστασίου Κωνσταντίνος

Επιβλέπων Καθηγητής: Δρ. Σαρρής Ιωάννης

Αθήνα, Σεπτέμβριος 2024

University of West Attica

School of Engineering

Department of Mechanical Engineering

Diploma Thesis

_____

Hydrodynamic Analysis of a Marine Propeller in Open Water Conditions Using the Computational Code OpenFOAM

Anastasiou Konstantinos

Thesis Supervisor: Dr. Sarris Ioannis

Athens, September 2024

This thesis was successfully examined by the following examination committee:

A/α	Name	Rank	Digital Signature
1	Sarris Ioannis	Professor	
2	Filippas Evangelos	Assistant Professor	
3	Gerostathis Theodoros	Associate Professor	

Δήλωση συγγραφέα διπλωματικής εργασίας

Ο κάτωθι υπογεγραμμένος Αναστασίου Κωνσταντίνος του Παναγιώτη, με αριθμό μητρώου 19392008 φοιτητής του Πανεπιστημίου Δυτικής Αττικής της Σχολής Μηχανικών του Τμήματος Μηχανολόγων Μηχανικών, δηλώνω υπεύθυνα ότι:

«Είμαι συγγραφέας αυτής της διπλωματικής εργασίας και ότι κάθε βοήθεια την οποία είχα για την προετοιμασία της είναι πλήρως αναγνωρισμένη και αναφέρεται στην εργασία. Επίσης, οι όποιες πηγές από τις οποίες έκανα χρήση δεδομένων, ιδεών ή λέξεων, είτε ακριβώς είτε παραφρασμένες, αναφέρονται στο σύνολό τους, με πλήρη αναφορά στους συγγραφείς, τον εκδοτικό οίκο ή το περιοδικό, συμπεριλαμβανομένων και των πηγών που ενδεχομένως χρησιμοποιήθηκαν από το διαδίκτυο. Επίσης, βεβαιώνω ότι αυτή η εργασία έχει συγγραφεί από μένα αποκλειστικά και αποτελεί προϊόν πνευματικής ιδιοκτησίας τόσο δικής μου, όσο και του Ιδρύματος. Παράβαση της ανωτέρω ακαδημαϊκής μου ευθύνης αποτελεί ουσιώδη λόγο για την ανάκληση του πτυχίου μου».

Ο Δηλών:

Αναστασίου Κωνσταντίνος

Acknowledgements

Contents

1 Abstract / Περίληψη

The constant growth of computing power the last years, has rendered the use of Computational Fluid Dynamics (CFD) extensive in the marine industry. For the purpose of meeting the greater requirements in efficient ship propulsion with low emissions and noise level as the International Maritime Organization (IMO) regulations demand, optimal propeller designs are expected. The open water test is performed as a means of obtaining characteristics important for the propeller design, and it is traditionally conducted using model tests in towing tanks. According to MEPC. 351(78) – 2022, numerical simulations (CFD) can be used complementary to model tests, of fully replace them.

The aim of the present thesis is the investigation and evaluation of the open-source CFD code OpenFOAM, that is suitable for the propeller's open water characteristics calculation. Initially, the motivation behind this study is presented which is the reduction of emissions in shipping as well as the assessment of underwater noise caused mainly by the propeller function. Consequently, the main framework of Regulations is outlined, on which the fidelity of the methodology used is based. The thesis continues with a brief historical review of the propeller and a presentation of the most commonly used numerical methods for designing and analyzing propellers. In Chapters 3 and 4, the basic theory behind this study is presented. Chapter 3 includes information about the propeller geometry and the open water characteristics, and Chapter 4 introduces the main hydrodynamic and numerical theory background. The study continues with the numerical simulation process which is analyzed in Chapter 5. Initially, the propeller model is selected, and the CAD model is created. Consequently, the set-up of the simulation and the mesh generation are conducted. The mesh independence study verifies that the calculated values are not dependent on mesh fineness. Afterwards, in terms of validating the methodology, the values are compared with official bibliographic data and with EFD (Experimental Fluid Dynamics) test results. For further validation, visualization figures are also presented, providing a clear sight of the calculated values. The study is coming to an end by discussing the results and some considerations for future work.

Λόγω της συνεχούς αύξησης της υπολογιστικής ισχύος, τα τελευταία χρόνια γίνεται εκτεταμένη χρήση της υπολογιστικής ρευστοδυναμικής στην ναυτιλιακή βιομηχανία. Οι σχεδιασμοί των ναυτικών ελίκων αναμένεται να είναι βέλτιστοι, ώστε να εκπληρωθούν οι απαιτήσεις της ενεργειακά αποδοτικής ναυτικής πρόωσης με χαμηλά επίπεδα εκπομπών ρύπων και υποθαλάσσιου θορύβου, όπως διατάσσουν οι κανονισμοί του Διεθνούς Οργανισμού Ναυσιπλοΐας (IMO). Η δοκιμή ελεύθερης ροής της έλικας είναι απαραίτητη για την απόκτηση χαρακτηριστικών που είναι απαραίτητα για τον σχεδιασμό και παραδοσιακά διεξάγεται σε υδατοδεξαμενές, με τη χρήση δοκιμών μοντέλων. Σύμφωνα με την απόφαση MEPC. 351(78) – 2022, οι αριθμητικές προσομοιώσεις (CFD) μπορούν να συμπληρώσουν η να αντικαταστήσουν την χρήση δοκιμών μοντέλων για τον υπολογισμό της έλικας σε ελεύθερη ροή.

Ο στόχος της παρούσας εργασίας είναι η χρήση και η επικύρωση του ανοικτού κώδικα OpenFOAM, για τον υπολογισμό των χαρακτηριστικών της έλικας σε ελεύθερη ροή. Αρχικά παρουσιάζονται τα κίνητρα της μελέτης, που είναι η μείωση των εκπομπών ρύπων και του υποθαλάσσιου θορύβου -που προέρχεται κυρίως από την λειτουργία της έλικας- από τη ναυτιλία. Ακολούθως, περιγράφεται το κύριο κανονιστικό πλαίσιο, βάσει του οποίου καθορίζεται η πιστότητα της μεθοδολογίας που χρησιμοποιείται. Η μελέτη συνεχίζεται με μια σύντομη αναφορά στη ιστορία της ναυτικής έλικας και με μια ανασκόπηση στις κύριες μεθόδους σχεδιασμού και ανάλυσης των ελίκων. Στα κεφάλαια 3 και 4, παρουσιάζεται το βασικό θεωρητικό υπόβαθρο της μελέτης. Το κεφάλαιο 3 περιλαμβάνει πληροφορίες για την γεωμετρία της έλικας και για τα χαρακτηριστικά αυτής σε ελεύθερη ροή, ενώ το κεφάλαιο 4 εστιάζει στην θεωρία υδροδυναμικής και αριθμητικών υπολογισμών. Η μελέτη συνεχίζεται με την διαδικασία της αριθμητικής προσομοίωσης, που αναλύεται στο κεφάλαιο 5. Αρχικά επιλέγεται το μοντέλο της έλικας και δημιουργείται η CAD γεωμετρία. Κατόπιν, διεξάγεται η ρύθμιση της διάταξης της προσομοίωσης και η δημιουργία του πλέγματος. Η μελέτη ανεξαρτησίας του πλέγματος, επιβεβαιώνει πως οι τιμές που υπολογίζονται δεν εξαρτώνται από την πύκνωση του. Έπειτα, αποσκοπώντας στην επικύρωση της μεθοδολογίας, οι τιμές συγκρίνονται με επίσημα βιβλιογραφικά και πειραματικά (EFD) δεδομένα. Για επιπλέον επαλήθευση, παρουσιάζονται στιγμιότυπα με οπτική αναπαράσταση των τιμών. Στο τέλος της εργασίας, σχολιάζονται τα αποτελέσματα και συζητούνται προτάσεις για μελλοντική εργασία.

2 Introduction

2.1 Motivation

Shipping companies will have urgent need for more energy-efficient vessels in the upcoming years in order to comply with the new regulations set by the International Maritime Organization (IMO) and the European Union's Green Deal, which targets a reduction in emissions by at least 55% by 2030. To achieve this, the overall improvement of the ship's hydrodynamic efficiency is essential, necessitating the design of optimal propellers for greater efficiency, see, e.g., Anevlavi et al (2023). Additionally, commercial vessels play a significant part in the background noise contribution in the sea, with propellers being a primary source of shipping noise. In response, IMO has recently issued guidelines, targeting on decreasing the noise emitted under the sea by commercial ships, for the cause of mitigating adverse effects on marine ecosystems, see e.g., Belibassakis & Politis (2019). Today, Computational Fluid Dynamics (CFD) is a standard practice for addressing these issues.

2.1.1 Emission Reduction

The temperature of the earth has risen by 1.1 °C in contrast to levels before the industrial age. The Paris Agreement in 2016 outlined the threshold of 1.5 °C as the first limit, which is expected to be reached in the midst of 2033 and 2035, see e.g., UN, Paris Agreement (2015). Furthermore, even under the most hopeful scenarios, a 2°C rise is anticipated by middle of this century, regardless of all the striving attempts to prevent this outcome, see e.g., Diffenbaugh et al (2023). Just 2.89% is the shipping contribution in the total human-caused greenhouse gas (GHG) emissions, see e.g., Faber et al (2020). Notwithstanding the latter fact, even the smallest progress in reducing carbon emissions can have a meaningful impact, since the severe and undeniable effects of global warming have turned into significantly evident. The International Maritime Organization (IMO) has worked extensively and has achieved great progress in the last years, for the purpose of decarbonizing the maritime industry, see e.g., Bilgili et al (2024).

The GHG (Greenhouse Gases) Strategies are pivotal outputs in the journey towards decarbonization. The IMO published the Initial GHG Strategy in 2018,

which was in line with the objectives of a Roadmap. According to this Roadmap, the Initial GHG Strategy would be assessed and revised by 2023. Indeed, the updated GHG Strategy was adopted in July 2023., see e.g., Bilgili et al (2024).

The Initial IMO Strategy was crafted in agreement with the conventions of the United Nations on the Paris Agreement, the Framework Convection of the United Nations on Climate Change (UNFCCC), the Law of the Sea (UNCLOS), and the Sustainable Development Group of the United Nations, underscoring IMO's crucial role in the formulation, adoption, and implementation of environmental regulations. The first GHG Strategy was aiming to the IMO's efforts enhancement in global GHG emission reduction consistent with Sustainable Development Goal (SDG) 13, identifying relevant procedures and measures, as appropriate to helping the accomplishment of the aforementioned objectives, consisting of research, advancement and keeping track of international shipping's GHG emissions.

Five years had passed since the release of the Initial GHG Strategy, and IMO had already developed deeper insights into the issues and was prepared for enhanced action. The 2023 GHG Strategy emerged from this encouragement and eagerness, see e.g., Bilgili et al (2024). According to IMO's revised strategy, the maritime sector is working to identify the best methods for cutting greenhouse gas emissions and moving toward a zero-emission future. This endeavor involves modernizing aging fleets and transitioning to carbon-neutral fuels amid a complex array of green technologies. Since there is not a single, effective way to decarbonize the maritime sector, a variety of strategies, such as switching to carbon-neutral fuels, increasing energy efficiency, slowing ships down, and optimizing logistics, have a great deal of potential to significantly reduce emissions.

According to the 2023 GHG Strategy, among the measures to enhance energy efficiency, improving the overall ship hydrodynamic performance is key. These improvements allow ships to consume less fuel to cross the same mileage, thereby reducing carbon dioxide and other GHG emissions. Enhancing a ship's hydrodynamic performance involves various modifications that decrease water resistance, making it more efficient. A fundamental enhancement is also optimizing the propeller design. A critical aspect of this is the propeller's open water test, which is an experimental procedure that assesses a propeller's

performance in ideal conditions, separate from the hull. This test is essential for determining the propeller's efficiency, see e.g., Bacalja et al (2024).

The most comprehensive assessment of a new ship's power requirements and the most accurate prediction of its hydrodynamic performance are achieved by conducting model hull and propeller experiments in a towing tank. Various tests are conducted to evaluate ship resistance, propulsion, maneuverability, and seakeeping for all hull forms, see e.g., Wartsila Encyclopedia of Marine and Energy Technology (2024). While traditional ship model tests still provide more accurate performance predictions than current CFD methods, CFD offers many advantages that make its study and application essential, see e.g., Windgrove (2014). CFD enables the simulation of conditions that are challenging or impractical to replicate physically, allowing for the testing of multiple scenarios. Additionally, it offers detailed insights into fluid flow, covering areas difficult to measure in experimental tests, such as velocity or pressure distribution and turbulence. Moreover, once set up, CFD simulations can be run repeatedly with varying parameters, saving time and resources in the long term, see e.g., Louisiana State University, CFD Simulations.

2.1.2 Noise Assessment

An increasingly recognized important and pervasive pollutant, impacting marine ecosystems globally, is the underwater noise emitted from ships, see e.g., Underwater Noise, EMSA (2024). Over the past 50 years, measurements have indicated a rapid increase in ocean noise levels, primarily due to the rising number, size, and speed of ships, see e.g., Belibassakis & Politis (2019). The frequency range of noise emitted by commercial vessels can interfere with critical frequencies used by various marine species, potentially masking their natural sounds and causing adverse effects, see e.g., Regan (2023). This issue is especially problematic for cetaceans, which are highly vocal and rely on the noise they produce for communication, locating food, reproduction, detecting predators, and navigation.

The primary sources of underwater noise from ships include the propeller functioning in cavitating as well as in non-cavitating conditions, mechanical equipment such as main and auxiliary engines, and the movement of the hull

through water, see e.g., EMSA (2024). Propeller noise, particularly under cavitating conditions, is the main contributor to noise emitted from ships.

The International Maritime Organization (IMO) released guidelines in an effort to lessen the underwater noise that commercial ships emit, and by that way protecting marine life. These recommendations offer technical guidance to shipbuilders, designers, and operators on how to reduce the underwater noise that ships emit, see e.g., IMO MEPC.1/Circ.833 (2014). The greatest potential for reducing underwater noise lies in the ship's initial design phase. For existing vessels, achieving the same noise performance as new designs is generally impractical. Therefore, specific design considerations are primarily aimed at new ships, though they can also be adapted for existing ships when feasible. Although flow noise around the hull has a minimal impact on radiated noise, see e.g., AQUO (2015), the hull's shape affects the water flow to the propeller. In order to effectively reduce underwater noise, hull and propeller designs should have complementing roles. These parts of the design ought to be incorporated into the broader deliberations concerning ship safety and energy efficiency.

Underwater noise levels can be significantly increased due to cavitation, which is the primary source of radiated noise, see e.g., IMO MEPC.1/Circ.833 (2014). Thus, propellers should be designed and chosen to minimize it. The definition of propeller cavitation is worth mentioning: When a part of the propeller's blade is subject on a pressure field that is lower than seawater's vapor pressure, causing a phase change in the water, then the propeller is under cavitating conditions. When the vapor pockets formed in this low-pressure region move into a higher-pressure gradient, they collapse back into liquid, producing noise. There are certain types of cavitation that are mainly contributing to the propeller-generated underwater noise, including tip vortex, blade sheet, and hub vortex cavitation, see e.g., ABS Practical Consideration for Underwater Noise Control (2021).

Since predicting cavitation and measuring propeller acoustics are often challenging to be carried out in standard maritime experimental establishments, predictions conducted with computational calculations are significantly useful, see e.g., Loyd (2015) and Krasilnikov (2019). In the Rome 2008 Workshop on modelling propellers in cavitating conditions, results submitted by seven participating organizations make available an extensive

range of capabilities applied to marine propeller flow and cavitation modelling, see e.g., Salvatore (2009).

2.1.3 Regulatory Framework

Numerical Calculations first appear on AIACS Recommendation No. 173 (November 2022) - Guidelines on Numerical Calculations for the purpose of deriving the V_{ref} in the framework of the EEXI Regulation. According to the aforementioned recommendation, the IMO (International Maritime Organization) is putting into action immediate steps to increase ship energy efficiency and lessen fuel consumption in an effort to minimize shipping's carbon emissions. One of these metrics is the Energy Efficiency Existing Ship Index (EEXI), which was implemented on January 1, 2023. The in-service vessel's efficiency is evaluated from the EEXI framework as they are designed and constructed. The calculation of EEXI is conducted in agreement with the method outlined by the detailed IMO Resolution MEPC. 350(78) – 2022, Guidelines on the Method of Calculation of the Attained Energy Efficiency Existing Ship Index (EEXI).

The reference speed of the vessel (V_{ref}) is a key factor necessary for the EEXI calculation. According to the IMO resolutions MEPC.350(78) and MEPC. 351(78) Numerical Calculations are considered as an acceptable way to determine the V_{ref} in the framework of the EEXI regulation. Furthermore, a part of the process for deriving V_{ref}, is the propeller open water calculation which is traditionally conducted using model tests in towing tanks.

As per MEPC. 351(78) - 2022 Guidelines on Survey and Certification of the Attained Energy Efficiency Existing Ship Index (EEXI), for propeller open water calculations, numerical simulations may be used in addition to model tests, or completely replace them. Accordingly, the following points are noted in the sequence of this subsection, which relates to presenting the level of requirement when numerical calculations are used for these purposes:

1. The guidelines below should be followed for conducting the numerical calculations:
   ITTC 7.5-03-01-02, Rev.02, 2021
   ITTC 7.5-03-01-04, Rev.00, 1991
   ITTC 7.5-03-03-01, Rev.00, 2011

2. The settings of the Boundary and fluid domain conditions must be proper, so they have no effect on the obtained results. The report that the provider will issue should include documentation of this.

3. The following deviations from the definitions and requirements in section 6 of AIACS Rec. No. 173 (Nov 2022) are permitted: Propeller models must be BEM (Boundary Element Method) models at the very least and on account of that, actuator disk or force models are not acceptable.

4. A validation report for the suggested methodology on a propeller that is equivalently similar (such as the Wageningen-B series) may be included in the report in replacement to the requirements outlined in section 7.6 of AIACS Rec. No. 173 (Nov 2022). In the relevant propeller operating range, the discrepancies between the numerical and expected results should not exceed 3% (comparison on the basis KT, 10KQ, and η).

2.2 State of the Art Review

2.2.1 Premature Research

A brief historic review concerning the early development of the screw propeller will be presented according mainly to the more detailed bibliographic study of John Carlton (2018).

One of the earliest hydraulic machines, the screw pump was first considered to be used as a means of propelling ships, according to the thinking of the ancient Greek engineer Archimedes (287–212 BC). In that way, he provided to future engineers involved in marine propulsion research, significant inspiration.

About 1700 years later, in the late 1480s, the Italian engineer Leonardo Da Vinci (1452–1519 A.C.) presented a different kind of screw propulsion through his studies, based on the idea of applying fan blades with resembling features to the ones used for cooling purposes today. Specifically, he describes in his sketchbooks a concept for a flying machine that would use air as the working fluid rather than water and have an aerial screw or spiral rotor according to the water screw design.

The work by Robert Hooke (1635–1703 A.C.) who was an English polymath, laid the foundation for the screw propulsion development as it is today known. Due to his keen interest in metrology, Hooke designed in the course of his work an air flow meter based on a windmill design. In 1683, he successfully modified this device to measure water currents. He then envisioned how this invention could be used to propel ships through the water if driven by a suitable motive power source. The device consisted of four flat, rectangular blades that were angled toward the plane of rotation and mounted on radial arms.

The Swiss Mathematician and Physicist Daniel Bernoulli (1700-1782 A.C.) presented the propeller wheel in 1752, a device which he aspired to operate along with a Newcomen steam engine and propel a ship at 2.5 knots by applying 20 – 25 hp. For his design he was awarded with a prize by the Academy of Sciences in Paris.

Around the same time as Bernoulli, the French mathematician Alexis-Jean-Pierre Paucton (1736–1798 A.C.) was conducting research and presented an alternative design that was based on the Archimedean screw.

Thirty years later, the English inventor Joseph Bramah (1748 – 1814 A.C.) introduced a design that incorporates the majority of the characteristics associated with screw propulsion nowadays, with the screw propeller located at the stern of a vessel. It was made up of a horizontal shaft that extends past the hull beneath the waterline and a propeller with a small blade number.

Some years later, in 1802 the English engineer Edward Shorter (1767-1836) modified Bramah's design to support sail crafts at calm winds and to help them further advance forward. In Shorter's arrangement, the shaft was designed to pass through the internal of the vessels hull, higher than the waterline, and therefore excluded the sail necessity.

Monsieur Dollman, introduced in 1824 in France, the first contra-rotating propeller design. His configuration consisted of a pair of windmill-style propellers with contrary rotational directions on a single shaft axis.

Subsequently, the Swedish–American engineer John Ericsson, who is considered the inventor of the screw propeller along with Francis Pettit Smith, designed a propulsion system in 1836 which included two contra-rotating propeller wheels, where eight short blades were attached to the tips of each

wheel by a peripheral strap. His design allowed a vessel to achieve a good propulsion result and a top speed of about 8.7 knots. Nevertheless, the Admiralty board was disappointed because the propeller's placement behind the rudder had a negative effect on the ship's steerability and the propeller flow, which led to Ericsson's departure from England to the United States. He designed the Princeton, the first screw-propelled ship in the US Navy, in 1843.

The English inventor Francis Petit Smith (1808-1874) at about 1840 presented a form of propeller similar to the Archimedean screw, yet having the significant asset to be installed on a different location in reference to the rudder. After fitting a wooden screw of two turns on a prototype boat and conducting trials, the Admiralty (the branch of the UK government in charge of leading the Royal Navy) responded sufficiently and motivated Smith into constructing a larger ship named Archimedes, which was equipped with two half-turn threaded screws. The results pleasantly surprised the Admiralty, who decided to adopt screw propulsion in the Royal Navy.

In 1838, Lowes designed a propeller consisting of one or more blades, each of which was a part of a curve that, when moved forward, generated a screw. Consequently, the s.s. Novelty was manufactured between 1839 and 1840 to evaluate the application of screw propulsion. In 1841, it made a voyage to Constantinople with 420 tons of cargo, and it can be regarded as the first cargo ship propelled by a screw propeller.

 By 1842, the windmill type propeller first introduced by Hooke in 1681, had evolved significantly compared to the Archimedean screw. The propeller installed on the ship Napoleon, with a displacement of 376 tons, is noteworthy for having undergone numerous model tests that varied the diameter, number of blades, blade area, and pitch before reaching its final design.

The ship Archimedes, previously mentioned, was lent to British civil and mechanical engineer Isambard Brunel (1806-1859), who tested it with a variety of propeller designs. Due to the results of Brunel's experiments on the Archimedes, the passenger steamship Great Britain changed the foregone means of propulsion that was paddle propulsion, to screw propulsion. Interestingly, the propeller design Brunel selected for Great Britain, did not follow Smith's propeller types but resembled Ericsson's design, although it's propeller type was not contra-rotating. Brunel's original propeller design was

later altered because it had a propensity to shatter while in use. Nonetheless, in practical terms, the pitch that was chosen was fairly similar to the one that would have been selected nowadays.

By January 1845, the testing of about thirty-two different propeller designs had been conducted. Smith's design proved to be the most efficient, enabling the ship to reach a speed of around nine knots. By March 1845, the Admiralty had ordered numerous smaller ships and seven screw-propelled frigates because they were so confident in the advantages of screw propulsion.

In the second half of the nineteenth century, theoretical methods for describing how the screw propeller functions were introduced. Theoretical contributions from Froude and Rankine were the most significant. These early propeller application practices and developments shaped the field as it is currently understood and practiced, and laid the foundation for the twentieth-century development of marine propeller technology. After the turn of the nineteenth century, propeller design advanced primarily in detailed aspects focused on improving efficiency and controlling cavitation, particularly concerning vibration and erosion.

2.2.2 CFD and Propulsion

Potential-based or panel CFD codes, along with RANS (Reynolds Averaged Navier Stokes) CFD codes, comprise the numerical methods typically employed for propeller performance design and analysis, see e.g. Anevlavi et al, (2023).

The Navier-Stokes Equations, which account as the foundation of almost all CFD problems, are used to describe many fluid flows. By removing the terms that describe viscous actions from these equations, the Euler equations are derived. The complete potential equations that describe the potential flow can be obtained by further simplifying the terms that describe vorticity. The potential flow or panel codes are developed using the potential flow assumptions.

Turbulent flows are mainly described by the time-averaged Navier-Stokes equations, also known as the Reynolds-averaged Navier-Stokes (RANS) equations. Unlike the panel methods, these equations account for viscous effects and for vorticity. Using approximations based on an understanding of

the turbulent flow properties, they can be used to provide approximate solutions that are averaged in time, to the Navier-Stokes equations.

The study by Brizzolara et al (2008) provides a comprehensive comparison between RANS and panel methods for propeller analysis in order to highlight the benefits and drawbacks of each method. In a broad range of advance coefficients, the thrust and torque coefficients can be calculated with sufficient accuracy (within 2-3%) for design purposes. Except for a small trailing edge region, the pressure distributions predicted by the two methods are notably similar along the blade at design advance coefficient and consistent with the experimental measurements. As anticipated, the RANS solver exhibits superior accuracy at low advance ratios, making it more appropriate for simulating heavily loaded propellers or in off-design scenarios where the potential flow solution begins to be severely conditioned by substantial viscous effects, boundary layer thickness (and ultimately separation) at the trailing edge and at the blade root and by intense secondary cross flows along the blade.

Both approaches demonstrate adequate accuracy and agreement with experiments when it comes to the induced velocities in the wake; however, they fall short in describing the tangential velocity increase and axial velocity decrease near the location where the helical vortex line is shed in the wake from the blade. Nevertheless, both methods provide sufficiently accurate calculations for engineering purposes for the primary hydrodynamic effects that might be necessary in order to investigate the hydrodynamic action of a propeller on a body submerged in its wake (like a rudder or, in the case of a contra-rotating system, another propeller).

One of the most used panel methods for propeller analysis is the lifting surface method. Numerical solutions for linearized propeller lifting-surface design problems fall into two categories. Firstly, there is the widely used vortex-lattice method, see e.g., Kervin (1978) and Greeley (1982). Secondly, there is a group of three-dimensional panel methods, see e.g., Kinnas (1996) and Belibassakis et al. (1998), which allow further improvement of formulations accounting for cavitation effects, see e.g., Fine and Kinnas (1993). At last, Anderson in 1997 studied the application of lifting-line and lifting-surface methods for the optimization of a propeller with a tip-fin and skew reformation, where towing tank experiments evaluated the optimization study's results.

3 Marine Propellers and Propulsion

3.1 Propeller Geometry

The complex geometry of the propeller demands a significant amount of information to be fully described. Therefore, the basic parameters that are correlated with this study will be introduced and explained in this section.

The traditional propeller design is conducted using systematic propeller series (e.g. Wageningen B-Series), see e.g., Politis G. (2015, 2019). For the development of these series some geometrical parameters are used which are related to the hydrodynamic performance of the propeller. These parameters are:

    1. The Propeller Diameter (D)
    2. The Nominal Pitch (P) (usually at r/R=0.7)
    3. The Blade Number (Z)
    4. The Expanded Area Ratio (A_E/A_0)

Since the terms diameter (D) and blade number (Z) have obvious meanings, the other two parameters, Pitch (P) and Expanded Area Ratio (A_E/A_0) are clarified below.

The propeller blade is defined about the reference line, which is a line normal to the shaft axis. A series of airfoil sections that are defined on the surface of cylinders whose axes are concentric with the shaft axis make up the propeller blade, see e.g., Carlton (2018). These sections are referred to as cylindrical sections. The shape of this section allows significant lift force with a small amount of drag force. This cylindrical definition of the section is depicted in Figure 3.1, where it is evident that the section is obliquely positioned over the cylinder's surface. As a result, the nose tail line of the airfoil section which connects it's leading and trailing edges, forms a helix around the cylinder's surface. As described in propeller technology, the term Pitch (P) refers to the advance distance of the helical line along the cylindrical surface, after a full rotation, see e.g., Politis (2015). The Pitch Angle (θ) is defined as: $\theta = \tan^{-1}\left(\frac{p}{2\pi r}\right)$. In figure 3.2 the pitch distance is defined for the blade section at the radial station r/R=0.7. This is usually referred to as Nominal Pitch.
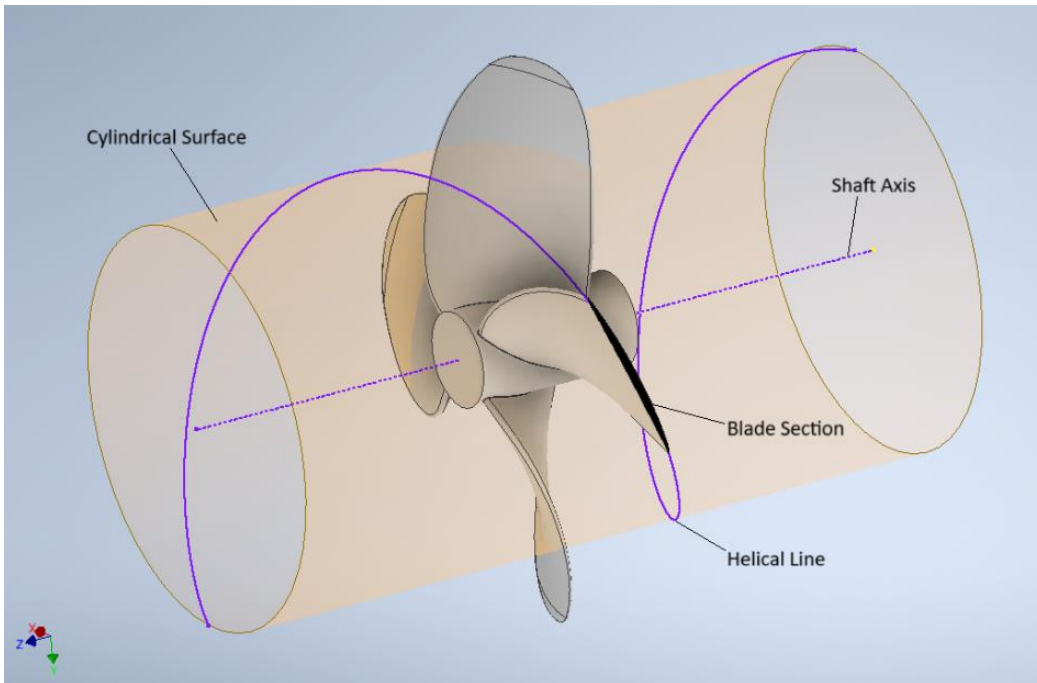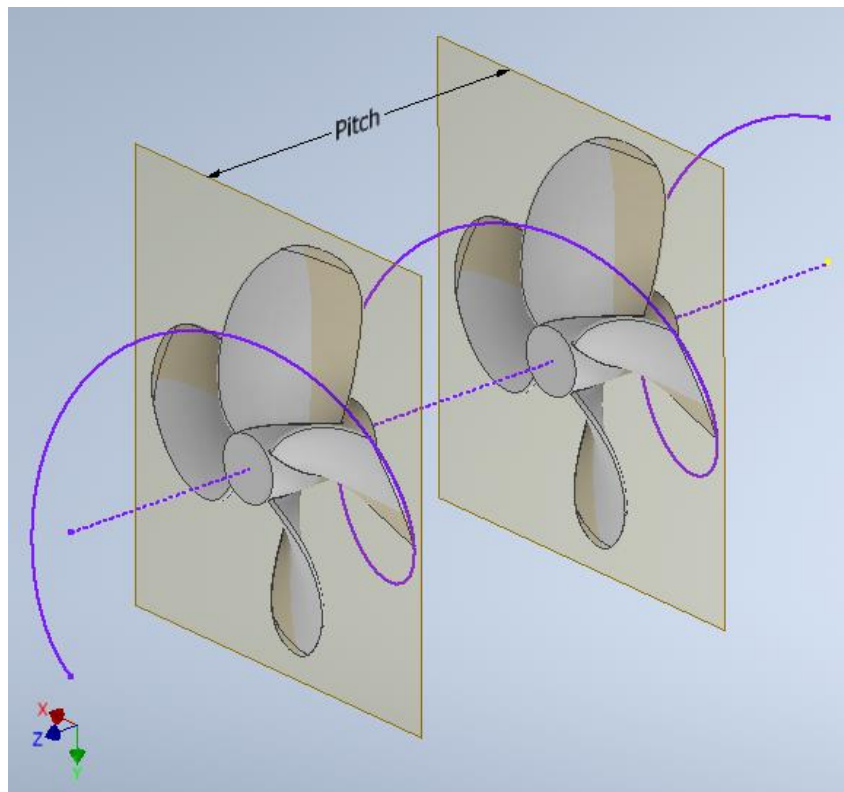
Figure 3.1 Cylindrical Blade Section Definition

Figure 3.2 Pitch Definition at r/R=0.7

The expanded outline can be defined as a depiction of the unwrapped cylindrical sections at their accurate radial stations about the blade reference line, see e.g. Njaastad et al, (2022). As seen in figure 3.3, at the left side, the projected outline which is the area in the plane normal to the thrust vector is plotted, and the unwrapped cylindrical sections at various radii (r/R) are presented. The corresponding sections defined along a flat plane (unwrapped) are displayed on the right side of figure 3.3. The propeller's hub radius is denoted by r_0, the propeller's total radius by R, and the radius of a random blade section by r. The expanded area of a propeller of Z blades, is calculated by the relationship:

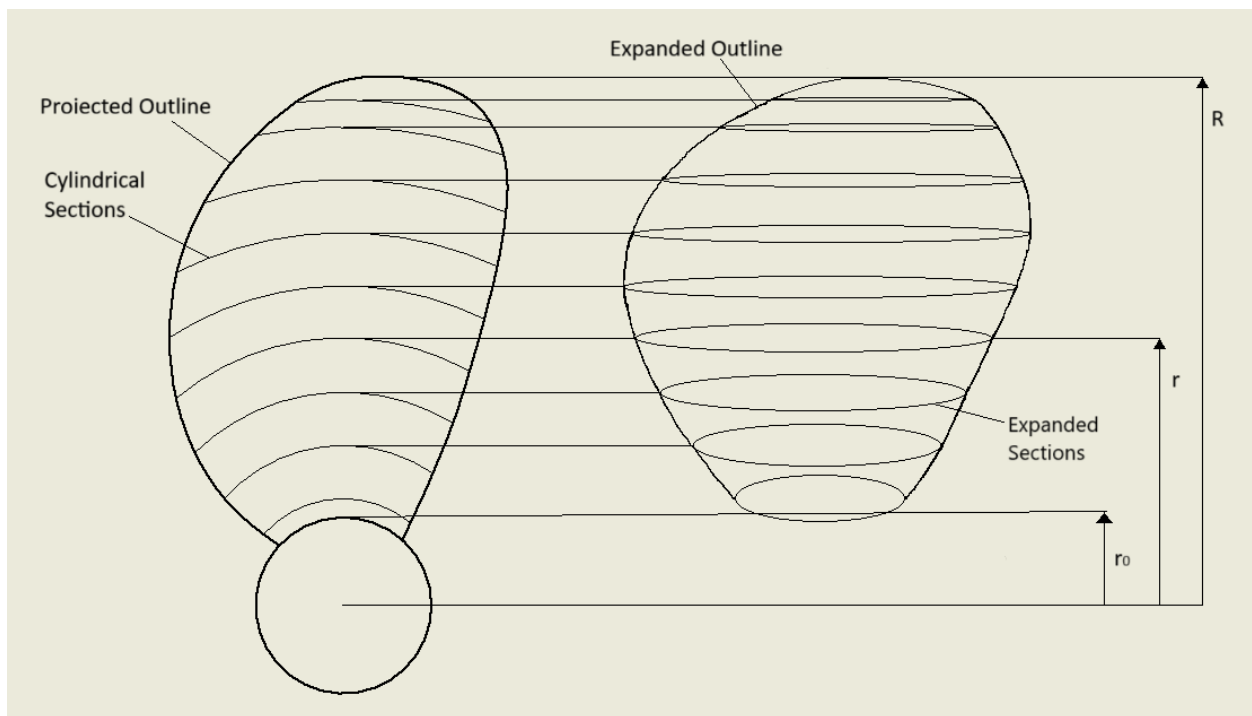$$A_E = Z \int_{r_0}^{R} c(r)dr \qquad (3.1)$$

Figure 3.3 Expanded Outline

The Expanded Blade Area Ratio is just the Expanded Area divided by the area of the propeller disc:

$$\frac{A_E}{A_0} = \frac{Z \int_{r_0}^{R} c(r)dr}{\frac{\pi d^2}{4}}$$

(3.2)

3.2 Propeller Open Water Performance Characteristics

The description of the forces and moments affecting the propeller when it operates in a fluid stream parallel to the shaft center line, which is also uniform, is where the open water characteristics are useful. The other category of performance characteristics that this study is not involved with is the behind-hull characteristics. The investigation of the aforementioned characteristics is conducted when a propeller located at the stern of a body is functioning in a mixed wake field, see e.g., Carlton (2018).

The thrust (T) produced by the propeller and the torque (Q) required to operate it, are measured to assess the propeller's performance in open water conditions, see e.g., Papakonstantinou (2019). Either an open water test, a cavitation tunnel or towing tank where the model-scale propeller operates under uniform flow conditions, or a CFD simulation are used to obtain these measurements. As shown in Figure 3.4, the experiment is typically carried out in the first scenario by advancing the propeller through the towing tank with a towing carriage.

Calculations are conducted at various operating points, which depend on the propeller's load and are typically controlled by adjusting the advance speed (V_A) while maintaining constant propeller revolutions. In the second case, the towing tank flow conditions are simulated in a computational domain, while the imported propeller geometry is created through a design software. This process is described in Chapter 5, and the theoretical background is presented in Chapter 4.

Figure 3.4 NTUA's Towing Tank, Set Up for Open Water Test, Ntouras et al (2022)

Below, the non-dimensional coefficients that represent the propeller's performance in open water are presented: The open water efficiency (η), the torque coefficient (KQ), and the thrust coefficient (KT). Within a range of advance coefficients J, these coefficients vary. These four coefficients are explained in the sequence of this section. Furthermore, it is necessary to note the existence of the other two basic open water numbers, not examined in this study: The Cavitation number (σ_{nD}), and the Weber number (W_{nD}).

3.2.1 Advance Coefficient (J)

The propeller advance ratio or coefficient is a dimensionless number used to describe the relationship between the speed at which a vessel is moving forward and the speed at which its propeller rotates, and is given by:

$$J = \frac{V_A}{nD} \tag{3.3}$$

Where, V_A (m/s) is the freestream (carriage) velocity, n (rps) the propeller's rotational velocity and D (m) the propeller's diameter.

To understand the physical meaning of the advance coefficient the following imagination is useful: An observer is standing at the propeller blade and is executing two motions simultaneously among with the blade: A translational motion with velocity V and a rotational motion with rotational velocity $\omega=\Omega r$. At this case, the observer standing at radius r, would see the water coming towards him with a velocity (V_A) resultant from the speed of advance (V) and the rotational speed (ω), see e.g. Politis (2019).

Figure 3.5 presents the expanded view of a section of the blade at radius r, among with the velocity triangle that is comprised by the velocities presented above. If φ is the angle of the resulting velocity (V_R), then:
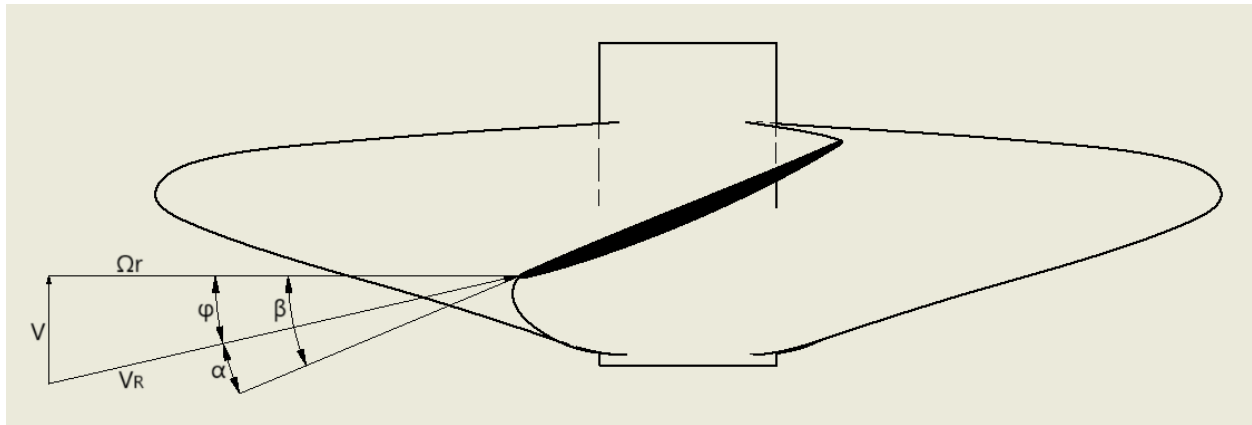

Figure 3.5 Velocity Triangle on a Blade Section

$$\tan \varphi = \frac{V}{\omega r} = \frac{V}{2\pi n r} = \frac{V}{\frac{2\pi n r}{R}R} = \frac{V}{nD\pi \frac{r}{R}} = \frac{J}{\pi \frac{r}{R}}$$

(3.4)

Therefore, the angle between the vector of the resulting velocity V_R and the horizontal axis is defined by the advance coefficient (J).

3.2.2 Thrust, Torque Coefficients (KT, KQ) and Efficiency (η)

The measured thrust (T) and torque (Q) are expressed as a function of the rotational speed (n) by applying dimensional analysis, assuming that free surfaces have no effect on the propeller performance:

$$K_T = \frac{T}{\rho n^2 D^4} \tag{3.5}$$

$$K_Q = \frac{Q}{\rho n^2 D^5} \tag{3.6}$$

Additionally, the ratio of the thrust horsepower (THP) to the delivered horsepower (DHP) is referred to as the open water efficiency (η), defined as:

$$\eta = \frac{THP}{DHP} = \frac{TV_A}{\omega Q} = \frac{TV_A}{2\pi n Q} = \frac{V_A \dfrac{T}{\rho n^2 D^4}}{2\pi n D \dfrac{Q}{\rho n^2 D^5}} = \frac{\dfrac{V_A}{nD}}{2\pi}\frac{K_T}{K_Q} = \frac{JK_T}{2\pi K_Q} \tag{3.7}$$

A propeller's open water diagram can be seen in figure 3.6, which presents the variation of KT, KQ and η (efficiency), versus the advance coefficient (J) and the pitch distribution (P/D), for the propeller investigated in the present study.
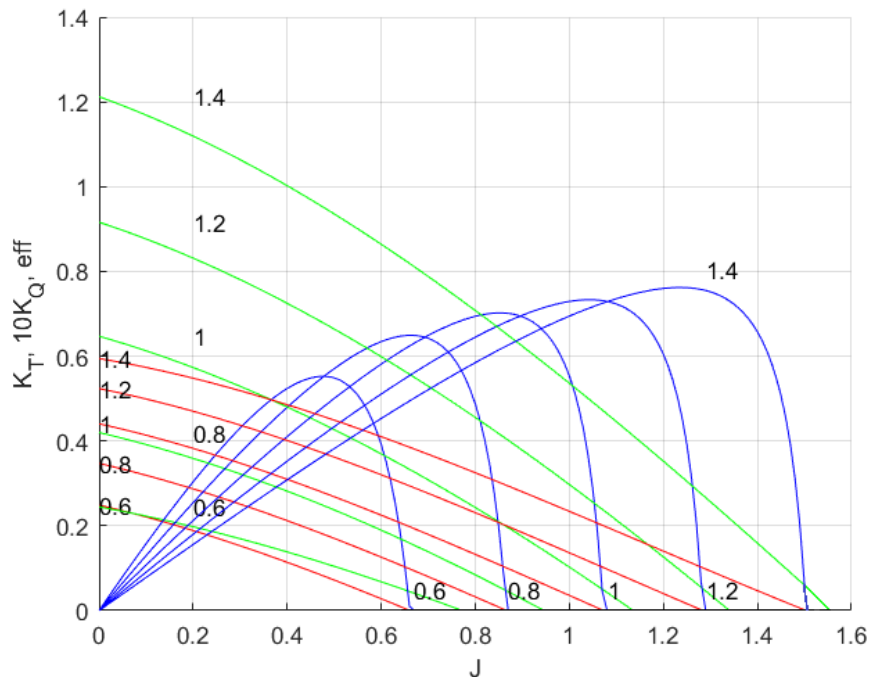

Figure 3.6 Open Water Diagram for Wageningen B4-0.628 Screw Series

27

3.3 Scale effects – Reynolds number

For the simulation conducted for this study, the Reynolds number has the constant value of $Re = 3.6 \cdot 10^6$ at the dimensionless radius r/R=0.75, and is calculated by the following equation:

$$Re_{75\%R} = \frac{V_{0.75R} C_{0.75R}}{v} \tag{3.8}$$

According to Politis (2019), the practice of scaled open water experiments while at the same time keeping the value of the advance coefficient (J) and the Reynolds number (Re) constant is impossible, due to experimental equipment inadequacy. Therefore, the under scale - open water test, is conducted with lower Re than the ship's and as a result the derived value of propeller efficiency (η) is lower than the real one at ship's scale. The latter point will be explained according to the diagram in figure 3.7.

At the following diagram in Figure 3.7, one can see the thrust and torque coefficient curves for two different Reynolds numbers:

- $R_n = 2 \cdot 10^6$ which represents the model scale
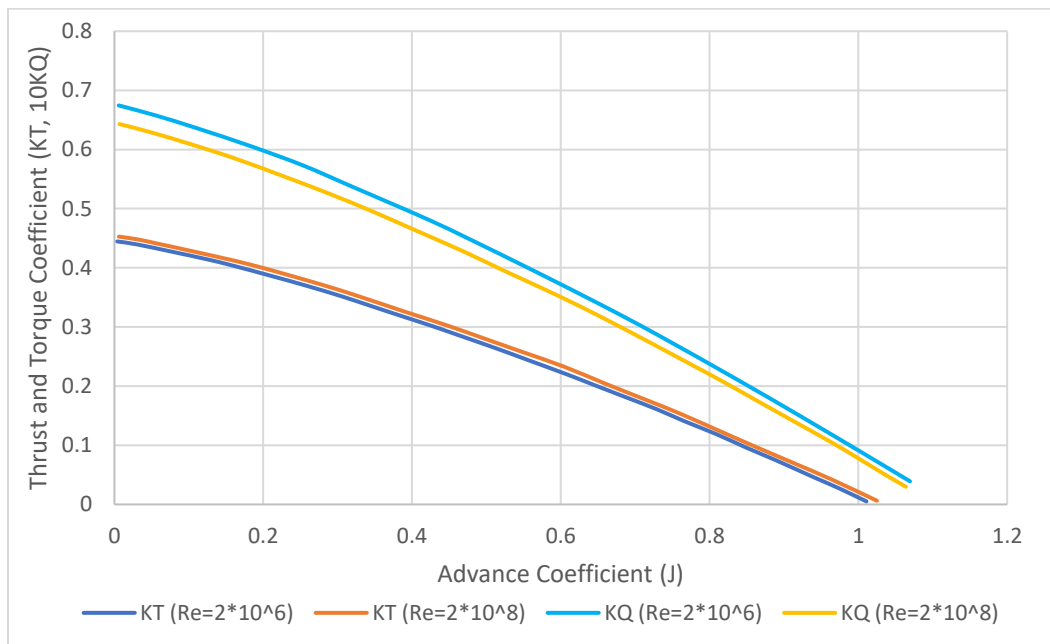- $R_n = 2 \cdot 10^8$ which represents the full ship scale

Figure 3.7 Reynolds Number Effect on KT and KQ, Carlton (2018)

As can be seen at the diagram above (Figure 3.7), the Reynolds number has a small, but not negligible effect on the coefficients. More specifically, by increasing Re, the thrust coefficient (K_T) increases, while the torque coefficient (K_Q) decreases. As a result, the efficiency (η) grows (see equation 3.7).

It is then obvious that calculations with scaled model experiments are conservative. In order to present non-conservative values for the vessel's speed, ITTC 7.5-02-03-04.1 describes guidelines for the correction of the Reynolds difference affected results, by using semi analytical methods based on the work of Lerbs (1951). In this study, the simulations are also conducted in model scale for the purpose of reducing the computational cost. According to AIACS No. 173 Rec. (2022) this practice is acceptable only if the scaling is performed following the ITTC 7.5-02-03-04.1 procedures.

4 Hydrodynamics and CFD of Propulsion

The introduction of the basic hydrodynamic and numerical theory behind this study is the purpose of the present chapter. It starts with the governing equations and consequently, essential information about the turbulence models is presented. Moreover, some fundamental numerical aspects will be also discussed.

4.1 Governing Equations

As all the mechanical systems, fluid dynamics are governed by conservation laws, specifically, the conservation of mass, conservation of momentum, and conservation of energy. However, in marine computational fluid dynamics (CFD), water is incompressible fluid, so the energy equation is not required for solution acquisition.

4.1.1 Conservation of Mass – Continuity Equation

The equation for the Conservation of Mass is specified as:

$$\frac{d\rho}{dt} + \rho(\nabla \cdot \vec{u}) = 0 \tag{4.1}$$

Where ρ is the density, $\vec{u}$ the velocity and ∇ the gradient operator.

$$\vec{\nabla} = \vec{\imath}\frac{\partial}{\partial x} + \vec{\jmath}\frac{\partial}{\partial y} + \vec{k}\frac{\partial}{\partial z} \tag{4.2}$$

Since the flow is incompressible: $\frac{d\rho}{dt} = 0$, and the continuity equation reduces to:

$$\nabla \cdot \vec{u} = \frac{\partial u}{\partial x} + \frac{\partial v}{\partial y} + \frac{\partial w}{\partial z} = 0 \tag{4.3}$$

4.1.2 Conservation of Momentum – Navier-Stokes Equation

$$\overbrace{\frac{\partial}{\partial t}(\rho\vec{u})}^{I} + \overbrace{\nabla(\rho\vec{u}\vec{u})}^{II} = \overbrace{-\nabla p}^{III} + \overbrace{\nabla \cdot (\bar{\bar{\tau}})}^{IV} + \overbrace{\rho\vec{g}}^{V} \tag{4.4}$$

Where p is the static pressure, $\bar{\bar{\tau}}$ is the viscous stress tensor and $\rho\vec{g}$ is the gravitational force per volume unit. Here, the roman numerals denote:

I: Local change with time

II: Momentum convection

III: Surface force

IV: Diffusion term

V: Source term

Viscous stress tensor ($\bar{\bar{\tau}}$) can be specified as below in accordance with Stoke's Hypothesis:

$$\tau_{i,j} = \mu \frac{\partial u_i}{\partial x_j} + \frac{\partial u_j}{\partial x_i} - \frac{2}{3}(\nabla \cdot \vec{u})\delta_{ij} \tag{4.5}$$

Where δ_{ij} is the Kronecker Delta:

$$\delta_{ij} = \begin{cases} 1, & if \ i = j \rightarrow Normal \ stress \ component \\ 0, & if \ i \neq j \rightarrow Shear \ stress \ component \end{cases} \tag{4.6}$$

Since the fluid is incompressible with constant viscosity coefficient μ the Navier-Stokes equation (4.4) simplifies to:

$$\rho \frac{D\vec{u}}{Dt} = -\nabla p + \mu \nabla^2 \vec{u} + \rho \vec{g} \tag{4.7}$$

4.2 RANS and Turbulence Modelling

If the Navier Stokes equation represented above gets averaged in time, it takes the following tensor form:

$$\frac{d(\rho U_i)}{dt} + \frac{d(\rho U_i U_j)}{dx_j} = -\frac{\partial P}{\partial x_i} + \frac{d}{dx_j}\left[\mu\left(\frac{\partial U_i}{\partial x_j} + \frac{\partial U_j}{\partial x_i}\right) - \overline{\rho u_i' u_j'}\right] \tag{4.8}$$

Equation (4.8) is called RANS (Reynolds Averaged Navier Stokes) equation, where:

U: Mean flow velocity

$\boldsymbol{u'}$: Velocity fluctuation due to turbulence

μ: Molecular viscosity

$-\overline{\rho u_i' u_j'}$: Reynolds Stress term

The averaging process results in the addition of the Reynolds Stress term to the equation, which has the mean flow quantities expression, for the purpose of solving the RANS equations.

By employing the Eddy viscosity hypothesis/ Boussinesq hypothesis the Reynolds stress term is solved:

$$-\overline{\rho u_i' u_j'} = \mu_t \left(\frac{\partial U_i}{\partial x_j} + \frac{\partial U_j}{\partial x_i} - \frac{2}{3} \frac{\partial U_k}{\partial x_k} \delta_{ij} \right) - \frac{2}{3} \rho k \delta_{ij} \qquad (4.9)$$

Where $\boldsymbol{\mu_t}$ is the turbulent or eddy viscosity.

Equation (4.9) is a combined equation for the shear and normal components of Reynolds stresses. If equation (4.9) is observed, it is realized that the solution of the RANS equation (4.8) can be achieved once the turbulent viscosity (μ_t) is calculated.

Therefore, the usefulness of the various turbulent models is the calculation of turbulent viscosity.

4.3 k-Ω SST Turbulence Model

F.R. Menter first introduced the SST k-ω (k-omega SST) in 1994. The k-ω and k-ε turbulence models are combined in this model. Therefore, before the k-omega SST model is presented, the k-ω and k-ε will be introduced and compared.

The k-ω and k-ε are both two equation models. In other words, they resolve two transport equations that take into consideration historical effects such as

turbulent energy diffusion and convection. Turbulent kinetic energy (k), the first of the two transported variables, is related to the determination of the energy in turbulence. The second variable is different in the cases of k-epsilon and k-omega. More specifically:

The turbulent dissipation rate (ε), or the rate at which viscosity converts turbulent kinetic energy into thermal energy, is the second transported variable in the k-epsilon case.

The specific turbulent dissipation rate (ω) is the second transported variable in the k-omega case.

The relation between dissipation rate (ε) $[m^2/s^3]$ and specific dissipation rate (ω) $[1/s]$ is given by:

$$\varepsilon = C_\mu k\omega \tag{4.10}$$

Where $C_\mu = 0.09$

The turbulent kinetic energy (k) is given by the transport equation below:

$$\frac{\partial(\rho k)}{\partial t} + \frac{\partial(\rho U_i k)}{\partial x_i} = \frac{\partial}{\partial x_i}\left[\left(\mu + \frac{\mu_k}{\sigma_k}\right)\frac{\partial k}{\partial x_i}\right] + P_k + P_b - \underbrace{\rho\varepsilon}_{Sink\ term} + S_k \tag{4.11}$$

Where,

$\boldsymbol{P_k}$: production of turbulent kinetic energy resulting from mean velocity shear

$\boldsymbol{P_b}$: production of turbulent kinetic energy resulting from to buoyancy

$\boldsymbol{S_k}$: source defined by the user

$\boldsymbol{\sigma_k}$: turbulent Prandtl number for k

As seen in equation 4.11, $\boldsymbol{\varepsilon}$ is a sink term, and within a flow it is expected to be high near walls and shear layers because there the dissipation of turbulence is expected to be high.

The turbulent dissipation rate (ε) is given by the following transport equation:

$$\frac{\partial(\rho\varepsilon)}{\partial t} + \frac{\partial(\rho U_i \varepsilon)}{\partial x_i} = \frac{\partial}{\partial x_i}\left[\left(\mu + \frac{\mu_t}{\sigma_\varepsilon}\right)\frac{\partial \varepsilon}{\partial x_i}\right] + C_1 \frac{\varepsilon}{k}(P_k + C_3 P_b) - C_2 \frac{\varepsilon^2}{k} + S_\varepsilon \quad (4.12)$$

Where,

C_1, C_2, C_3, C_μ are model coefficients that vary within k-ε turbulence models

S_ε: user-defined source

σ_ε: turbulent Prandtl number for ε

In the case of k-ω:

If equation (4.10) is substituted into the transport equation (4.12):

$$\frac{\partial(\rho\varepsilon)}{\partial t} + \frac{\partial(\rho U_i \varepsilon)}{\partial x_i} = \frac{\partial}{\partial x_i}\left[\left(\mu + \frac{\mu_t}{\sigma_\varepsilon}\right)\frac{\partial \varepsilon}{\partial x_i}\right] + \frac{\gamma}{v_t} P_k - \beta\rho\omega^2 + \underbrace{\frac{2\rho\sigma_\omega^2}{\omega}\frac{\partial k}{\partial x_j}\frac{\partial \omega}{\partial x_\iota}}_{Additional\ term} \quad (4.13)$$

As a part of substitution, an additional term appeared as seen in equation (4.13). In the absence of this term, equation 6 can be called as the specific turbulence dissipation rate (ω) transport equation.

To summarize, since ε and ω essentially represent turbulent dissipation, the two models are differentiated according to the different empirical model coefficients (α, β, β*, γ, σω, σk) they have.

In the case of k-ω the turbulent viscosity is calculated as:

$$\mu_t = \frac{\rho k}{\omega} \quad\quad\quad (4.15)$$

In the case of k-ε the turbulent viscosity is calculated as:

$$\mu_t = C_\mu \frac{\rho k}{\varepsilon} \quad\quad\quad (4.16)$$

Where C_μ is the turblence model constant (C_μ =0.09)

While the k-epsilon model typically performs well in the free stream region, the k-omega model is more accurate in the boundary layer region close to the wall. A blending function can be used to combine the benefits of these two turbulence models (figure 4.1). Consequently, the blending function is employed for the transition from the k-epsilon model at a distance from the wall (free stream region) to the k-omega model near the wall.
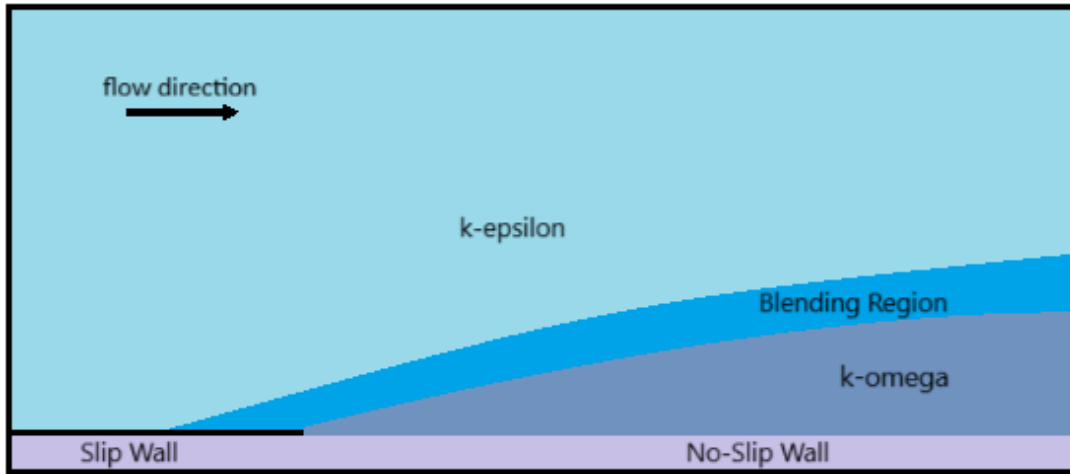

Figure 4.1 k-ω SST model switches between k-ω and k-ε using a blending function

If a function $(1-F_1)$ is multiplied with the additional term in equation (4.13), it takes the following form:

$$\frac{\partial(\rho\varepsilon)}{\partial t} + \frac{\partial(\rho U_i \varepsilon)}{\partial x_i} = \frac{\partial}{\partial x_i}\left[\left(\mu + \frac{\mu_t}{\sigma_\varepsilon}\right)\frac{\partial\varepsilon}{\partial x_i}\right] + \frac{\gamma}{v_t}P_k - \beta\rho\omega^2 + (1-F_1)\underbrace{\frac{2\rho\sigma_\omega^2}{\omega}\frac{\partial k}{\partial x_j}\frac{\partial\omega}{\partial x_i}}_{Additional\ term} \quad (4.17)$$

For cells away from the wall, $F_1 = 0$ so there is a remaining of the additional term, and equation (4.17) represents k–ε turbulence model because it is the transport equation for ε, used away from the wall.

For cells very close to the wall, $F_1 = 1$ so there is a vanishing of the additional term, and equation (4.17) represents k–ω turbulence model because it is the transport equation for ω used in a region very close to the wall.

For cells in the blending region, $0 \leq F_1 \leq 1$.

The calculation of turbulent viscosity for the k-omega SST model is conducted as follows:

$$\mu_t = \frac{a_1 \rho k}{\max(a_1 \omega, SF_2)} \tag{4.18}$$

Where F_2 is a different blending function, and S is the shear strain magnitude.

4.4 Discretization – Finite Volume Method

The Navier-Stokes equations are non-linear partial differential equations. These equations cannot be solved directly because of the presence of non-linear terms, so the employment of numerical methods is required, see e.g., Papakonstantinou, (2019). For the purpose of solving the equations, they must have a form that allows iterative solution, so their transformation into a set of algebraic linear equations is conducted. This can be accomplished in a number of ways, such as the finite difference method, the finite volume method, and the finite element method. The most popular CFD method, the finite volume approach, is employed in OpenFOAM. Several distinct finite volumes, referred to as cells, make up the computational domain. The governing equations are then integrated over each cell, and the Gauss divergence theorem is used to transform the integrals with the divergence term into surface integrals, see e.g., Polyzos (2017). The reformulation on each cell is then conducted, as a set of linear algebraic equations. Some important OpenFOAM terminology is presented before the fundamental principles for deriving the algebraic equations are introduced.

A typical OpenFOAM cell is illustrated in Figure 4.2. A set of cells that constitutes the computational domain should occupy the entire domain without overlapping. In the cell centers (P and N) the equations are being solved. Each cell is surrounded by multiple flat faces (f in Figure 4.2 - left) and with no limitations on the quantity or the orientation of the faces. This type of mesh is referred to as 'arbitrarily' unstructured.

One adjacent or neighboring cell, owns every face. A face is defined as illustrated in Figure 4.2 (right). Every face is a list of points that is arranged so that an edge connects any two nearby points. In Figure 4.2, the face normal vector S_f can be

seen. The right-hand rule determines its direction based on the point numbers on each face. A cell's volume is defined as V_P.
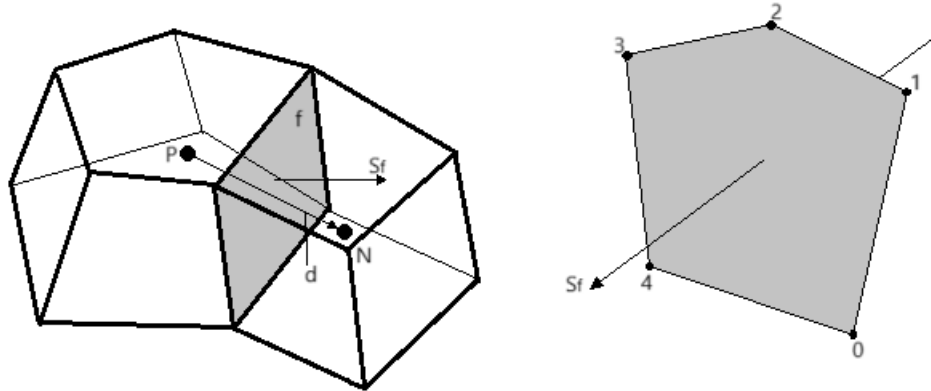

Figure 4.2 OpenFOAM Cell Definition (left), Face Definition (right)

Navier-Stokes equations have the form of a general transport equation. The discretization of the equations' terms is demonstrated using a this equation form. For a fluid property φ:

$$\frac{\partial \varphi}{\partial t} + \nabla \cdot (U\varphi) = \nabla(aU\varphi) + q_\varphi \qquad (4.27)$$

When integrating the equation over a control volume V, the following equation is derived:

$$\overbrace{\int_V \frac{\partial \varphi}{\partial t} dV}^{time\ derivative} + \overbrace{\int_V \nabla \cdot (U\varphi) dV}^{convection\ term} = \overbrace{\int_V \nabla(aU\varphi) dV}^{diffusion\ term} + \overbrace{\int_V q_\varphi dV}^{source\ term} \qquad (4.28)$$

The source term and the time derivative are simply integrated since they are just multiplied by the cell volume VP. The more precise Backward method or

the implicit Euler method can be used for approximating the time derivative, see e.g., Greenshields (2015).

The Gauss divergence theorem is employed, so that the convection and diffusion terms can be integrated. It can be expressed as:

$$\int_V \nabla * \varphi dV = \int_S \varphi * dS \tag{4.29}$$

Surface S encloses the volume V_P, φ is any tensor field and the $\nabla *$ symbols any tensor product. Specifically, $\nabla \times$: curl, or just ∇: gradient.

$$\int_V \nabla \cdot (U\varphi)dV = \int_S \varphi U \cdot dS \tag{4.30}$$

The approximation of the surface integral as the sum of discrete surfaces S_f, is conducted on the right part of the equation 4.30:

$$\int_V \nabla \cdot (U\varphi)dV = \int_S \varphi U \cdot dS = \sum_f \varphi U \cdot S_f \tag{4.31}$$

In order to obtain the discrete form of the transport equation, the same steps are performed for the diffusion term:

$$V_P \frac{\partial \varphi}{\partial t} + \sum_f \varphi U \cdot S_f = \sum_f (a\nabla\varphi) \cdot S_f + V_P q_\varphi \tag{4.32}$$

According to the notation used in Figure 4.2, the expression of the values of the variables $(\nabla\varphi, a, \varphi, U)$, is done by default in the cell centers (P, N). The variables must be expressed on the surfaces in order to evaluate the surface integrals in equation 4.32 above. Differencing schemes must be used in order to make this feasible. The differencing scheme is crucial for achieving the method's convergence. The following attributes should characterize any differencing scheme:

- Conservativeness
- Boundedness
- Trasportiveness

A thorough explanation of them can be found in the study of Polyzos (2017). Below, the schemes commonly used are briefly presented, see e.g., Greenshields (2015):

Central Differencing (CD) or Linear Interpolation an unbounded scheme with second-order accuracy. The variable on a face φ_f has a value as defined below:

$$\varphi_f = w\varphi_f + (1 - w)\varphi_N \tag{4.33}$$

Where w is a weight factor defined as $w = \frac{\overline{fN}}{\overline{PN}}$, $\overline{fN}$ is the distance between f and the cell center, and $\overline{PN}$ is the distance between the cell centers P and N.

Upwind Differencing (UD) determines φ_f according to the flow direction. This scheme is bounded at but has first-order accuracy. The upwind interpolation of φ_f is written as:

$$\varphi_f = \begin{cases} \varphi_p\, , & U_f \cdot S_f \geq 0 \\ \varphi_N\, , & U_f \cdot S_f < 0 \end{cases} \tag{4.34}$$

Blended Differencing (BD): In order to combine the benefits of both schemes; namely, the boundedness of the UD scheme and the accuracy of the CD scheme, blended differencing schemes combine the UD and CD schemes previously mentioned. The value of a variable on a face φ_f is defined as follows:

$$\varphi_f = (1 - \gamma)\left(\varphi_f\right)_{UD} + \gamma\left(\varphi_f\right)_{CD} \tag{4.35}$$

Where γ is a blending coefficient.

4.5 SIMPLE Algorithm

Pressure (P), and the three velocity components represented by the velocity vector (U), are the four unknown quantities of the Navier-Stokes equations. However, there are four unknowns and only three equations (the momentum formulation in x, y, and z). Therefore, an additional equation is required, which is the mass conservation equation. Since this equation does not include the pressure quantity, specific procedures are needed for the coupled pressure-momentum system to be solved. This is also known as the pressure-momentum coupling problem, see e.g., Holtzmann (2017).

For the purpose of the pressure equation derivation, the momentum equation in semi-discretized form is used, see e.g., Jasak (1996):

$$a_P U_P = H(U) - \nabla p \tag{4.36}$$

Where,

$$H(U) = \sum_N a_N U_N \tag{4.37}$$

Using equation 4.36, U can be expressed as:

$$U_P = \frac{H(U)}{a_P} - \frac{1}{a_P} \nabla p \tag{4.38}$$

The continuity equation has the following discretized form:

$$\nabla U = \sum_f S \cdot U_f = 0 \tag{4.39}$$

The expression of the velocities on the face of the cell is:

$$U_f = \left(\frac{H(U)}{a_P}\right)_f - \left(\frac{1}{a_P}\right)_f (\nabla p)_f \tag{4.40}$$

By substituting equation 4.40 to equation 4.39, the following equations is derived which accounts for the pressure equation:

$$\nabla \cdot \left(\frac{1}{a_P} \nabla p\right) = \nabla \cdot \left(\frac{H(U)}{a_P}\right) = \sum_f S \cdot \left(\frac{H(U)}{a_P}\right)_f \tag{4.41}$$

The incompressible Navier-Stokes system has the following discretized form:

$$a_P U_P = H(U) - \sum_f S \cdot p_f = 0 \tag{4.42}$$

$$\sum_f S \cdot \left[\left(\frac{1}{a_P}\right)_f (\nabla p)_f\right] = \sum_f S \cdot \left(\frac{H(U)}{a_P}\right)_f \tag{4.43}$$

These equations' form demonstrates the linear relationship between pressure and velocity. Special treatment of this inter-equation coupling is required. One can employ two primary methods: the segregated approach, in which the

equations are solved in order, and the simultaneous algorithms, which solve the complete systems of equations simultaneously over the entire domain. The first method is used in this thesis, with the SIMPLE algorithm.

Patankar and Spalding first introduced the SIMPLE (Semi-Implicit Method for Pressure Linked Equations) algorithm in 1972; see e.g., Patankar and Spalding (1972), Patankar (1980). It is commonly used for marine CFD applications and primarily for the case of steady state problems. For the purpose of ensuring stability and achieving a fast rate of convergence, the estimation of the relaxation factors for the fields and equations is of great importance. In figure 4.3 below, the basic steps of the algorithm are shown in a flowchart:
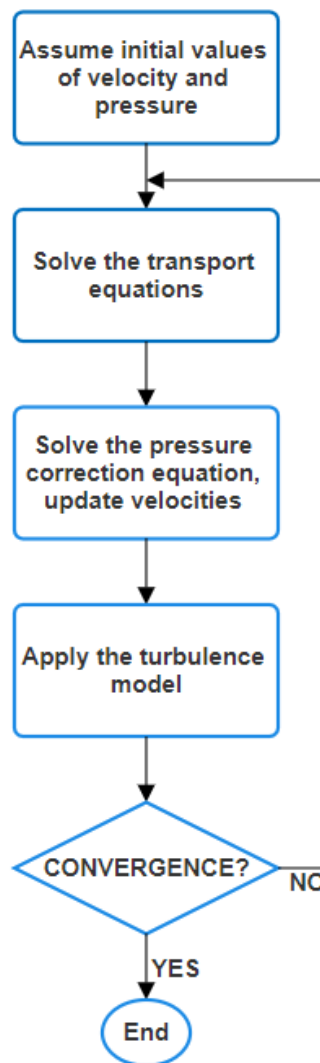

Figure 4.3 SIMPLE Algorithm Flow Chart

5 Propeller Open Water CFD Simulation

5.1 Selection of Propeller Model

For the cause of validation and evaluation of the open water simulation results, a Wageningen B-Series propeller model is chosen. This series, first introduced by Troost in 1940, see e.g., Troost (1940) is one of the most comprehensive and commonly used propeller models, see e.g., Carlton (2018).

The primary reason for selecting a B-Series model is the availability of open water curves, see e.g., Bernitsas et al (1981), which result from polynomials that are used for the expression of the thrust and torque coefficients in terms of the number of blades (Z), the blade area ratio (A_E/A_0) and the advance coefficient (J). These polynomials were derived from the multiple polynomial regression analysis of 120 propellers of the B-Series, tested at Netherlands Ship Model Basin (NSMB) in Wageningen, see e.g., Oosterweld and van Oossanen (1975). These open water curves will be compared with the ones derived from the CFD simulations using OpenFOAM, in terms of evaluation of the CFD process, as explained in chapter 2.1.3 Numerical Framework.

The secondary reason, is the availability of Experimental Fluid Dynamics (EFD) measurements that have been conducted for the same propeller model in the towing tank of Laboratory of Ship and Marine Hydrodynamics of the National Technical University of Athens (NTUA), see e.g., Ntouras et al (2022). This test was conducted to evaluate the in-house numerical code MaPFlow, developed at same laboratory, see e.g., Papadakis (2014). Both EFD and MaPFlow derived values will be compared with the OpenFOAM derived values.

5.2 CAD Model Generation

5.2.1 Geometry of Wageningen B4-0.628

The propellers of the Wageningen-B series are typically referred to by the notation BZ-y, where B stands for the 'B'-series, Z is the blade number and y is the blade's expanded area ratio (A_E/A_0), see e.g., Carlton (2018). Therefore, for the present study's model, Z=4 and A_E/A_0=0.628. Worth mentioning is that the direction of the propeller is right-handed when looking from the side of the

high-pressure values, it is in model scale, and it has the following basic characteristics presented at table 5.1.

Characteristic	Notation	Unit	Value
Diameter	D	m	0.16
Number of Blades	Z	-	4
Expanded Area Ratio	A_E/A_0	-	0.628
Pitch/Diameter Ratio	P/D	-	0.88
Skew Angle	θ_{eff}	degrees	24
Chord length at r/R=0.7	$c_{0.70}$	m	0.336608
Thickness at r/R=0.7	$t_{0.70}$	m	0.002496
Hub Diameter	D_h	m	0.0265
Direction of Rotation	-	-	Right-handed

Table 5.1 Basic Characteristics of Wageningen B4-0.628

The above characteristics are indicative for this model, and the well-rounded information about the geometry required for the generation of a Wageningen B-Series model can be seen in the work of Oosterveld and Ossannen (1975).

5.2.2 CAD Model Generation

In order to create a solid CAD model, suitable for CFD simulations, the CAESES Software developed by Friendship Systems A.G. is utilized. More specifically, for the generation of Wageningen B-Series propeller geometry, CAESES drives a web service, in which the user implements the geometrical blade parameters while having the ability of the model's direct visualization and can afterwards download the file at. STL or .STP format.

The geometry tool takes into account ISO standards for the various propeller settings. For the purpose of ensuring a high-quality surface, the tool involves internal optimizations for the blade characteristics calculation as well as special fine tuning to the B-Series profiles. The generated propeller consists of 2D profiles that are remarkably close to the B-Series definitions but can have a small deviation.

The geometrical values used for the generation of the CAD model, are presented in the following table 5.2:

Characteristic	Value	Unit
Propeller Diameter	0.16	m
Expanded Area Ratio	0.628	-
Pitch/Diameter Ratio	0.88	-
Number of Blades	4	-
Rake angle	0	degrees
Upstream Hub Diameter	0.0265	m
Downstream Hub Diameter	0.0265	m
Axial Hub Shift	0	m
Hub Length	0.048	m
Root Thickness	0.005856	m
Tip Thickness	0.00048	m
Leading Edge Fraction	0.198	-
Trailing Edge Fraction	0.1641	-
Size Hub Fillet	0.0048	-

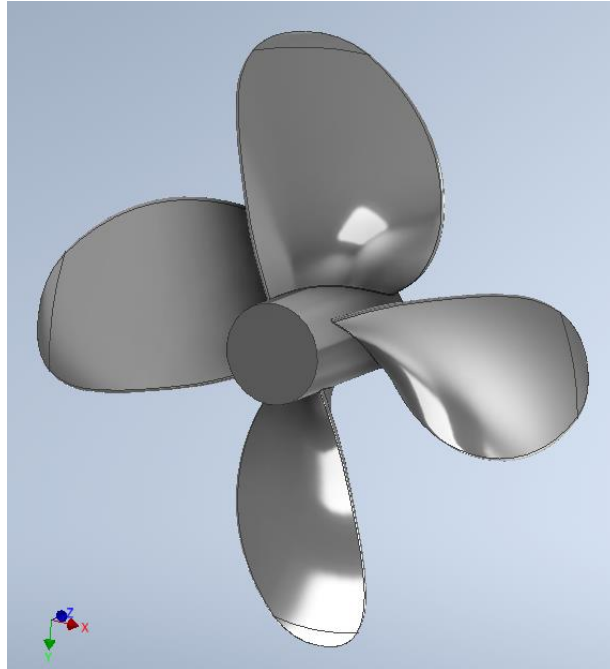*Table 5.2 Values Used for the CAD Model Generation*

Figure 5.1 Wageningen B4-0.628 CAD Model

Consequently, in order to create the final form of the CAD model, Autodesk Inventor software is utilized, and a propeller hub extrusion for two diameters downstream (L_h) of the flow is performed. The latter action occurred for the purpose of avoiding significant viscous effects downstream of the propeller, during the simulation, see e.g., Ntouras et al (2022). Additionally, the two sides of the hub are made round. The final CAD model is depicted in figure 5.2 below:
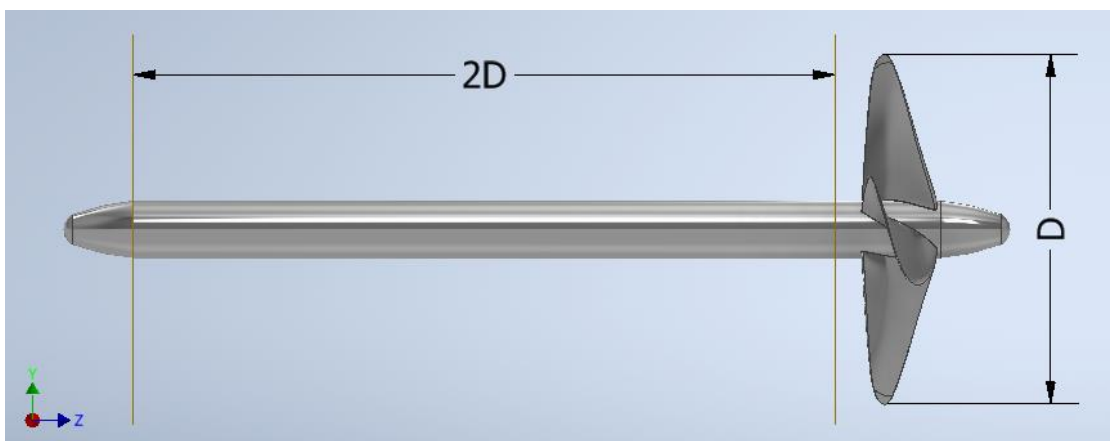

Figure 5.2 Downstream Hub Extrusion

5.3 CFD Software

SimScale is software product based on cloud computing, which allows computer-aided engineering (CAE) and was launched in 2013. Through SimScale, computational fluid dynamics (CFD), finite element analysis (FEA), thermal simulations etc., can be performed and was developed by SimScale GmbH. Open source and proprietary simulation codes are used by the backend of the platform. The open-source code, in the case of CFD is OpenFOAM.

Before describing the simulation process, it must be noted that the majority of the decisions made, and approaches followed in the simulation process are associated with the limited computational hours available. Therefore, regarding the factors that define the computational cost such as the mesh fineness, the limited computational resources available are taken into account, and maximum accuracy is attempted.

5.4 Simulation set-up

Before explaining the basic steps of the simulation set-up, it is noteworthy stating that the turbulence model is k-Ω SST, the time dependency Steady State, and the Algorithm used is SIMPLE.

5.4.1 Domain Size

The size of the computational domain plays a crucial role in influencing numerical results. Therefore, it should be defined in a way that ensures an uniform inflow upstream of the propeller and that prevents any downstream reflections, see e.g., Kalantzis (2020).

Based on the recommendation ITTC 7.5-03-03-01 (2014), The boundaries of the open water simulation's cylindrical computational domain must be positioned far enough from propeller center. In particular, the outlet boundary must be positioned at least 4D (D = propeller diameter) downstream, and the inlet boundary must be positioned at least 2D upstream. The outer boundary must be positioned at 4D or greater in the radial direction.

In this case, SimScale software has only the rectangular prism flow region extraction option available, therefore a rectangular prism with length of 44D,

height and width of 10D was created. While the outlet and outer boundary are positioned at a distance of 31D away from the propeller plane and axis, respectively, the inlet is positioned at a distance of 13D away from the propeller plane. In the following figure 5.3, the aforementioned dimensions can be seen. These are based on the work of Ntouras et al. (2022).
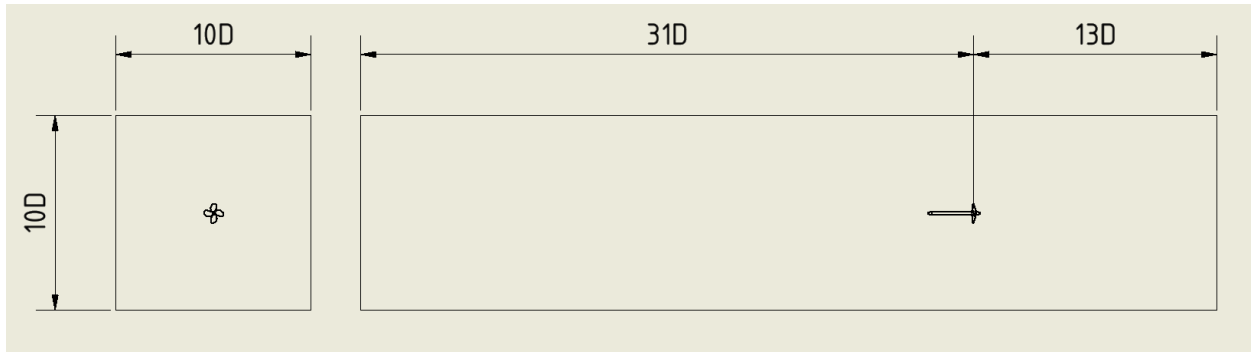

Figure 5.3 Computational Domain Dimensions

5.4.2 Boundary Conditions

The solution of fluid motion equations takes place within a boundary-restricted computational domain. The classical Dirichlet boundary conditions are used in the case of this study. The following table 5.3 presents the boundary condition types that are applied to each surface of the propeller geometry and to the geometry of the computational domain:

Surface	Boundary Condition
Flow Volume Inlet	Velocity Inlet
Flow Volume Outlet	Zero Pressure Outlet
Flow Volume External Walls	Slip Wall
Propeller Blades	No-Slip Wall
Propeller Upstream Hub	No-Slip Wall
Propeller Downstream Hub	Slip Wall

Table 5.3 Boundary Conditions

Regarding the boundary conditions assigned to the flow volume boundaries seen in figure 5.4, the inlet is assigned with a Velocity Inlet boundary condition, that defines a constant value, equivalent to the simulated advance velocity. The outlet is defined as a zero-pressure outlet. This setting indicates that the flow can freely exit the computational domain without imposing any artificial pressure constrains. Furthermore, the external walls are considered as slip walls, defining a zero-velocity normal to the boundary, while the parallel to the boundary velocity is left free.

When it comes to the propeller geometry boundaries seen in figure 5.5, the propeller blades surface and upstream hub surface are defined as no-slip walls, so there is a zero velocity normal to the boundary as well as a zero velocity parallel to the boundary. The turbulence wall is set as a full resolution turbulence wall. The downstream hub surface is considered a slip wall.
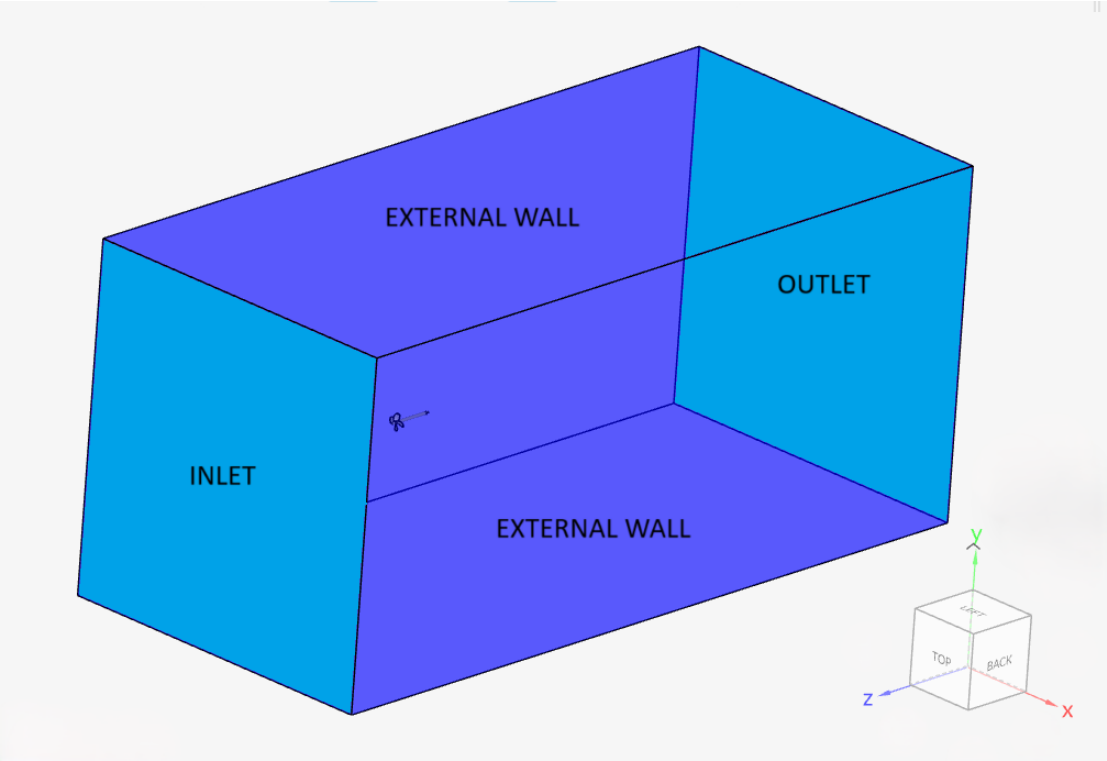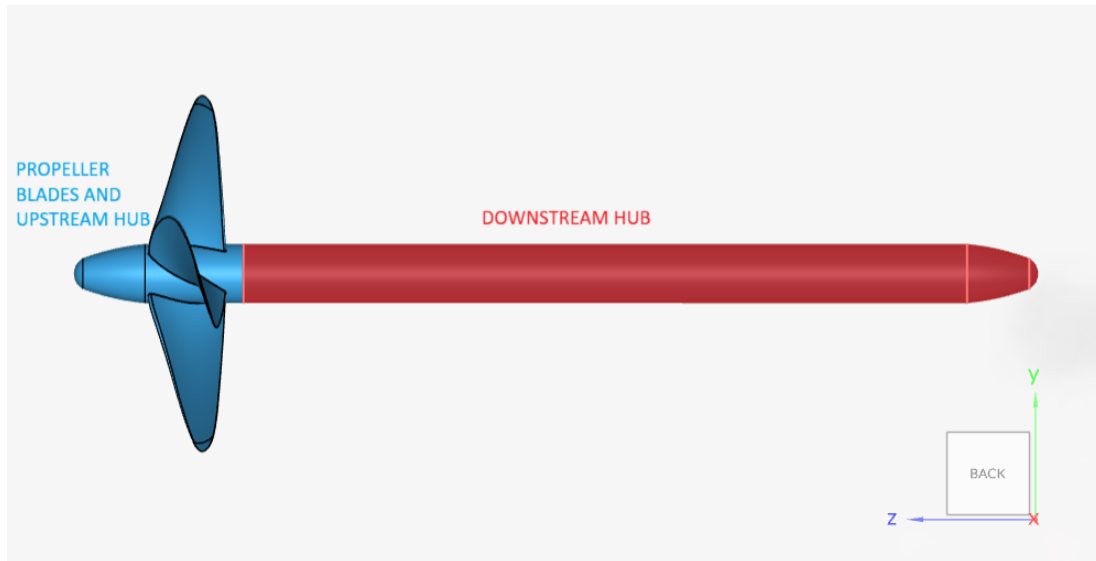

Figure 5.4 Flow Region Boundaries

Figure 5.5 Propeller Geometry Boundaries

5.4.3 Moving Reference Frame (MRF) Rotating Zone

In order to induce the rotation of the propeller a Moving Reference Frame (MRF) rotating zone is used, in accordance with the ITTC 7.5-03-03-01 (2014) guidelines. A steady-state approximation of the transient rotating motion at a particular "instance" of time is the MRF rotating zone. Consequently, there is no physical rotation of the propeller. The governing equations in the rotating zone are modified by this method, which makes use of a rotating frame of reference. Comparing MRF simulations to transient modeling, the former requires significantly less computing power. Therefore, MRF offers good approximations with less computational effort and significantly less computation time if the simulation is set up correctly.

The dimensions of the cylinder used as MRF for the current study are based on Simscale documentation and can be seen in figure 5.6. The z-axis is set as axis of rotation and the value of rotational velocity is set $\omega=1131$ rpm and is kept the same for all simulations, since the advance coefficients will change due to the variation of the freestream velocity at the inlet.
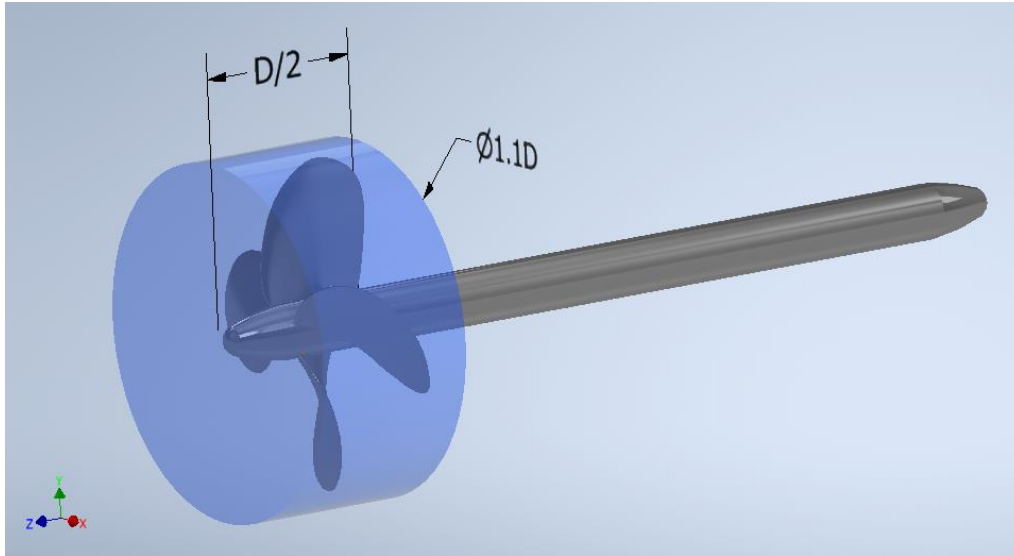
Figure 5.6 MRF Zone Dimensions

5.4.4 Flow Conditions

The selection of the flow conditions for the open water simulation is done for the purpose of matching the ones used for the towing tank experiment in the NTUA's Laboratory of Ship and Marine Hydrodynamics, conducted for the study of Ntouras et al. (2022). In that way, a constant Reynolds number at r/R=0.75 $(Re_{0.75} = 3.6 * 10^6)$ of the blades is achieved. As seen in the following table, constant value of rotational velocity is kept at $n = 18.85\ rps$, while the speed of advance (V_A) is altered in a range from 0.4 to 0.9.

Water density	ρ	kg/m^3	997.3
Kinematic Viscosity	ν	m^2/s	$0.93 \cdot 10^{-7}$
Number of revolutions	n	$1/s$	18.85
Advance Velocity	V_A	m/s	$0.4 - 0.9$

Table 5.4 Flow Conditions

5.4.5 Mesh Generation

To discretize the computational domain the standard meshing algorithm of Simscale is utilized. The operation type of the standard mesher uses a finite volume mesher. A three-dimensional unstructured mesh is generated by this tool that uses primarily hexahedral or tetrahedral elements.

For the purpose of conducting Grid Independence Study, three different grids are generated (coarse, medium, fine), whose size decreases with a reduction factor of at least $\frac{1}{\sqrt{2}}$ according to the ITTC recommendation 7.5-03-01-04 (1999).

The sizing is controlled by decreasing the edge size of the cells of specific surfaces and regions (volumes), by means of applying the proper refinements, as seen in table 5.5. The Region Refinement is used to refine the volume mesh for volume regions, while the Local Element size is applied to surfaces of the CAD model.

For the purpose of avoiding the use of a fine mesh for the places that don't require it, local refinement was applied only in a region around the propeller, and on the propeller geometry itself. Therefore, one cylinder called Wake Region was created around the propeller as depicted in figure 5.7. Another region where the mesh gets even denser is the MRF Zone. The propeller blade mesh and the hub upstream of the flow is comprised of even smaller cells and the tips and leading and trailing edges get a further cell size reduction. Additionally, the physics-based meshing option is enabled, which refines the mesh close to the walls, after taking into account the boundary conditions. This option in this study is mainly useful in terms of refining the cells close to the propeller blade and upstream hub walls.

Furthermore, three boundary layers are placed on the propeller wall by setting an overall relative thickness of 0.4, and a growth rate of 1.5, and the mesh node is placed 0.01mm away from the blade tip surface. This layer management resulted in $y^+ < 7$ on the blade tips, the leading and the trailing edge, and $y^+ < 15$ on the rest of the blade surface. A greater number of thinner layers should be created in order to accurately capture the boundary layer information, but this practice was not feasible due to the limited computational resources.

The downstream hub does not require mesh fineness, so the size of its cells is kept the same as the rest of the flow region for the three cases. The rest of the flow regions cells are sized by setting the fineness bar at 6, same for the three grids, and the average edge size results 0.05m.

First, a coarse grid is created by setting maximum edge length to specific surfaces and regions as seen in table. These length values are divided by $\sqrt{2}$ to create the medium mesh, and similarly the values of the medium mesh cell edges length are divided again by $\sqrt{2}$ to create the fine mesh.
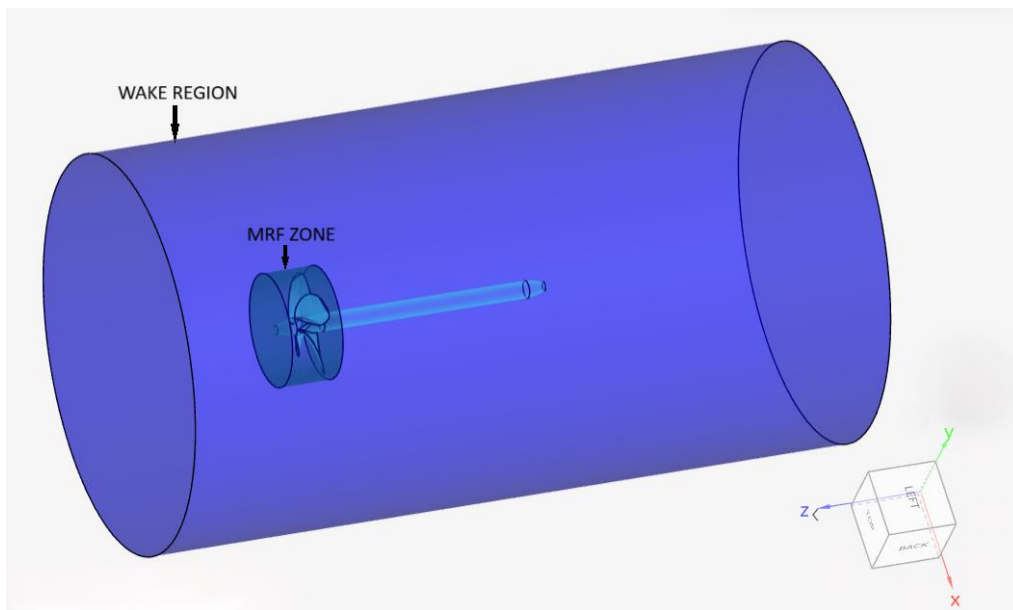
Figure 5.7 Mesh Refinement Regions

Surfaces and Regions	Refinement Type
Propeller Blade Surfaces	Local Element Size
Propeller Upstream Hub Surface	Local Element Size
Propeller Blade Tips	Local Element Size
Propeller Blade Leading and Trailing Edges	Local Element Size
MRF Zone	Region Refinement
Wake Region	Region Refinement

Table 5.5 Refinement Types

Surfaces and Regions	Maximum Edge Length (m) – Coarse Mesh	Maximum Edge Length (m) – Medium Mesh	Maximum Edge Length (m) – Fine Mesh
Propeller Blade Surfaces	0.0015	0.001061	0.00075
Propeller Upstream Hub Surface	0.0015	0.001061	0.00075
Propeller Blade Tips	0.0004	0.0002828	0.0002
Propeller Blade Leading and Trailing Edges	0.0004	0.0002828	0.0002
MRF Zone	0.003	0.00212	0.0015
Wake Region	0.035	0.02	0.01

Table 5.6 Maximum Edge Length Settings for the Three Meshes

The grids generated have the following number of cells:

Mesh	Cell Number
Coarse	3.5M
Medium	5.6M
Fine	10.8M

Table 5.7 Cell Number of Each Mesh

As stated at the following chapter, due to grid convergence, the fine grid can be selected to continue the study. Therefore, the data and figures of the fine mesh will be presented in the sequence of this subsection.

Mesh Element	Number
Cells	10800000
Nodes	3885098
Edges	16491
Faces	24488449
Triangles	17261759

Volumes	10819865
Hexahedra	1780881
Pyramids	700057
Tetrahedra	7316248
Quadrangles	7226690
Prisms	1022679

Table 5.8 Mesh Element Numbers

Figure 5.8 Propeller Blade Mesh

In figure 5.8, one can see the refinement at the tip of the propeller blade as well as at the refinement at the leading and the trailing edge.
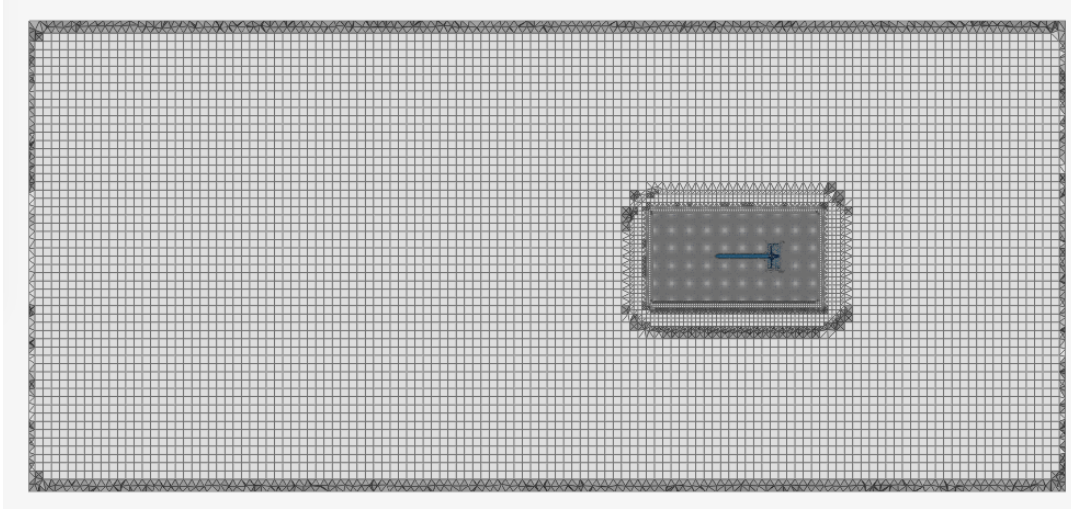
Figure 5.9 Flow Region Mesh

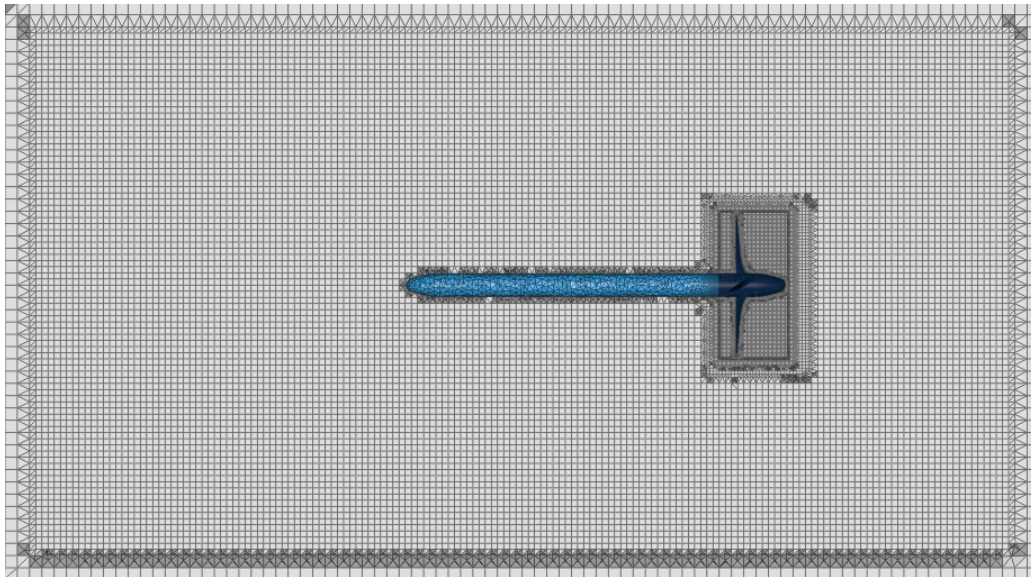In figure 5.9, the mesh of the entire computational domain is visible, as well as the refinement of the wake region.

Figure 5.10 Wake Region Mesh

In figure 5.10 one can see the mesh of the wake refinement region, as well as the MRF Zone refinement.
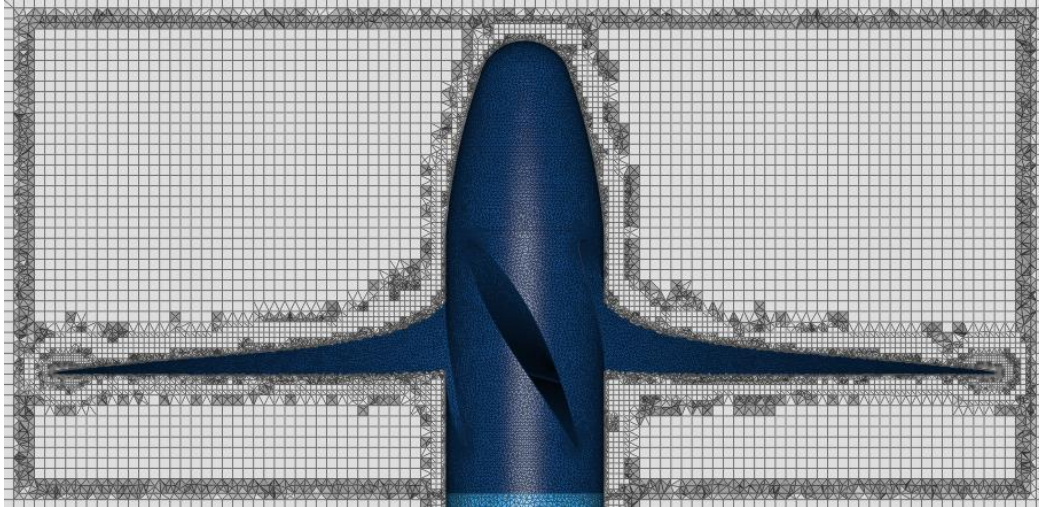
Figure 5.11 MRF Zone Mesh

In figure 5.11, the mesh of the MRF Zone, the propeller blades and the upstream hub, is visible. The refinement applied on the geometry surface and on the mesh near the no-slip wall, is obvious.
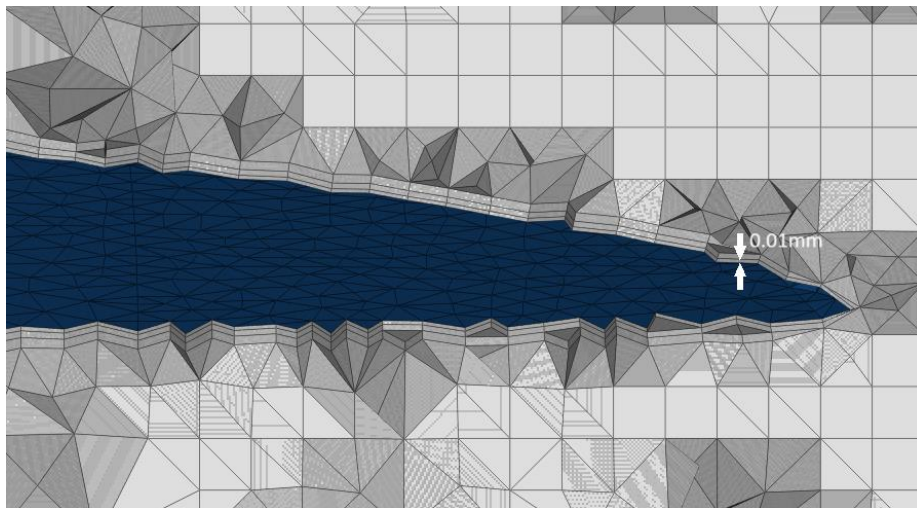
Figure 5.12 Layers Around Blade Tip (Thickness of First Layer)

The layers around the blade tip are visible In figure 5.12 and the thickness of the first layer is t=0.01mm, the y+ values achieved are less that 7 (see figure 5.16). For a more accurate boundary layer calculation, a greater number of

thinner layers should be used, but this practice would require more computational resources.
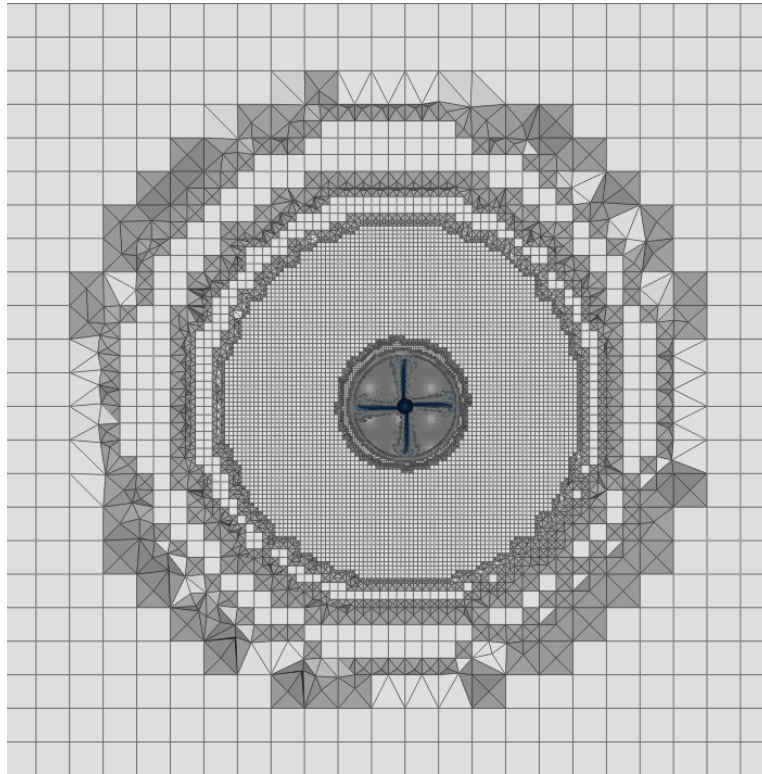

Figure 5.13 Flow Region Mesh (Sectional View)

In figure 5.13 the gradual reduction of the different mesh regions cell size can be seen.

5.5 Mesh Independence Study

The three simulations conducted for the Mesh Independence Study accounted for an advance coefficient (J) of 0.7. In the first simulation, 3.5 million cells that comprised the coarse mesh are used. The second one was conducted with the medium mesh that consisted of 5.6 million cells, and for the third one the fine mesh of 10.8 million cells was used. The derived KT and 10KQ values from each mesh are presented in table 5.9. The comparison of the KT and 10KQ values derived from the three simulations is shown in table 5.10.

	Coarse Mesh	Medium Mesh	Fine Mesh
KT	0.130751	0.1246747	0.123074
10KQ	0.220167101	0.214672137	0.216653878

Table 5.9 KT and 10KQ Values

	MEDIUM-COARSE	FINE-MEDIUM
δKT (%)	-4.873914267	-1.300522181
δKQ (%)	-2.559700436	0.923147667

Table 5.10 Relative Differences
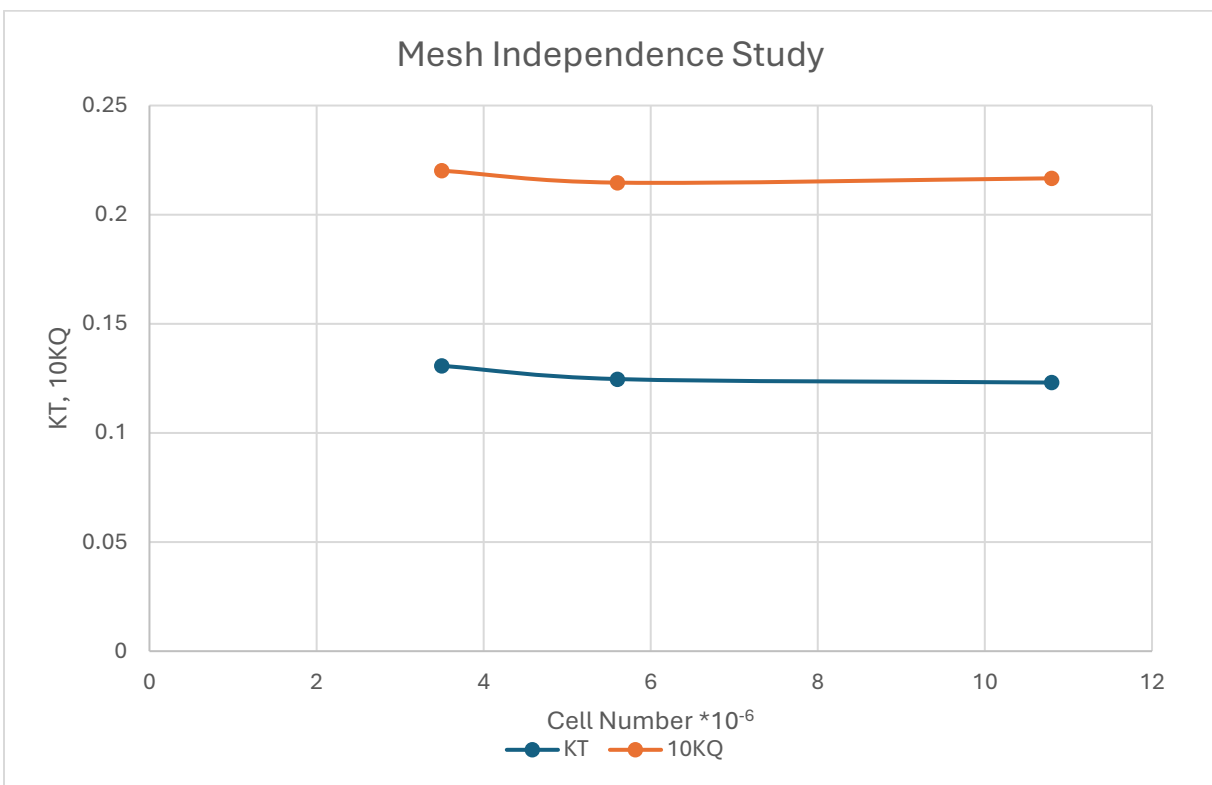
Figure 5.14 Change of KT and 10KQ by Cell Number

According to the values and the diagram above, since the difference between the results of the fine and medium mesh is minor, it is concluded that the size of the mesh does not influence the results of the simulations. Therefore, there is mesh independence, and the fine mesh is selected for the consequence of the study.

5.6 Convergence

The Residuals are presented in figure 5.14. The forces and torque values that are measured, are transformed afterwards into the coefficients of thrust and torque. In the diagrams below the aforementioned coefficients are presented, for advance coefficient J=0.7.
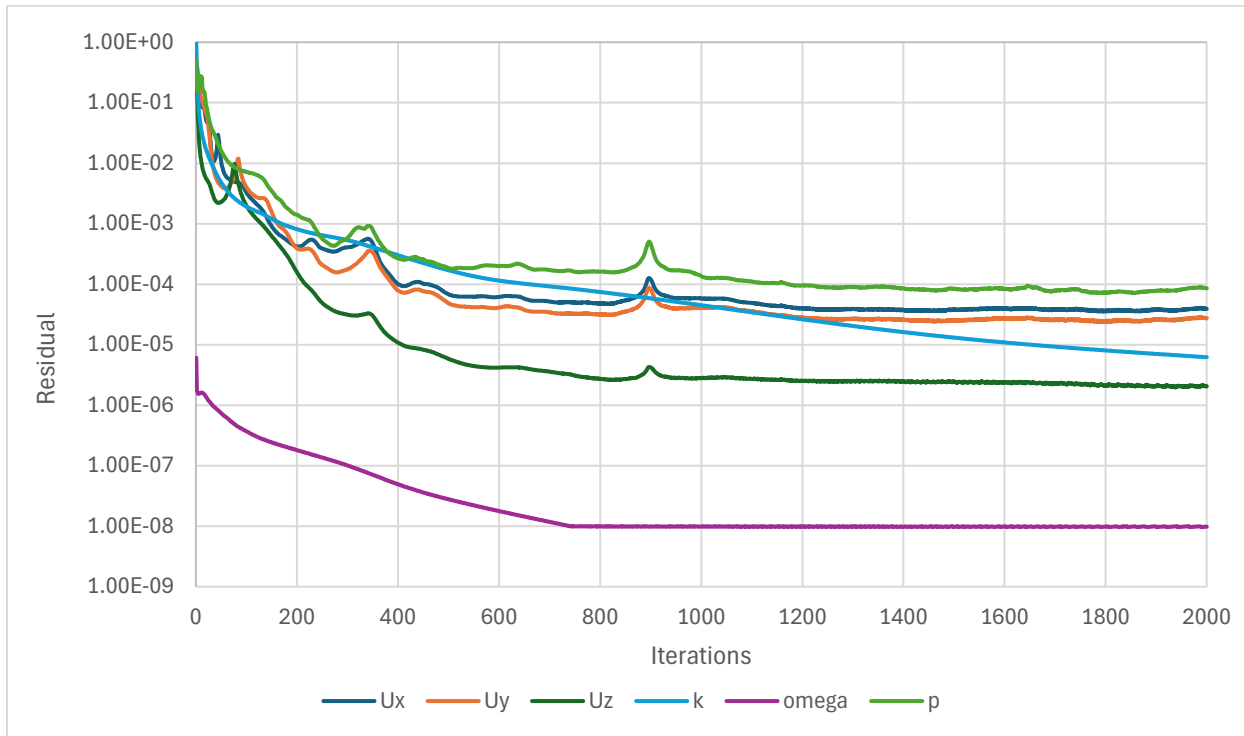

Figure 5.15 Residuals Plot

The Residuals plot in figure 5.14 shows sufficient convergence. If the simulation run endured longer, and more iterations were done, the convergence would have been better. This practice would nevertheless require more computational resources.
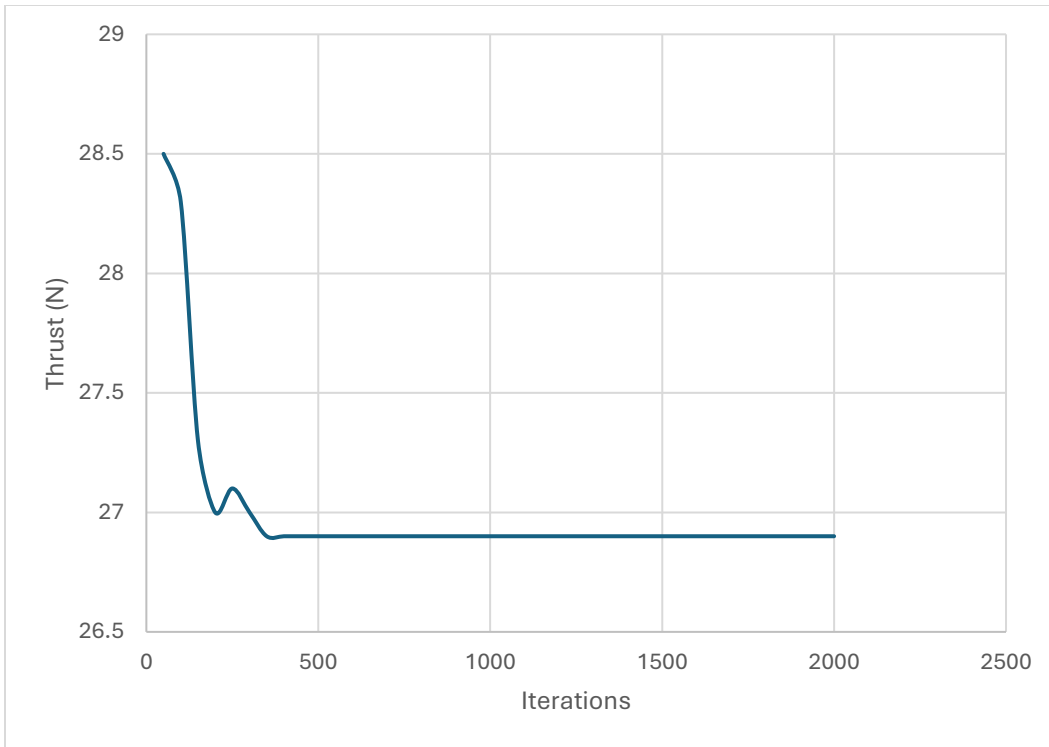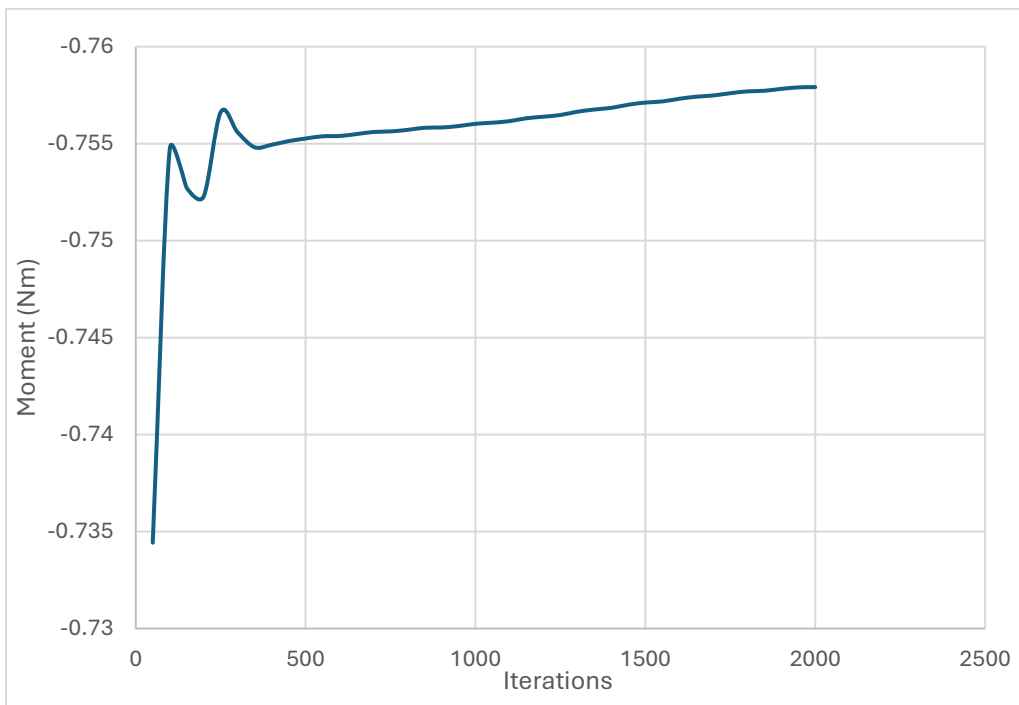
Figure 5.16 Thrust Plot

Figure 5.17 Moment Plot

5.7 Comparison with B-Series Polynomials data

A range of advance coefficients from J=0.4 to J=0.9 was used for the conduction of the simulations, and the calculated open water characteristics are then compared with the values resulting from the B-Series Polynomials.

J	KT (B-SERIES)	KT (OPENFOAM)	δKT%
0.4	0.2515	0.2678	-6.50%
0.5	0.2098	0.2222	-5.91%
0.6	0.1658	0.1736	-4.73%
0.65	0.1430	0.1481	-3.55%
0.7	0.1198	0.1231	-2.74%
0.8	0.0723	0.0722	0.16%
0.9	0.0239	0.0172	27.81%

Table 5.11 KT Comparison with B-SERIES Data

J	10KQ (B-SERIES)	10KQ (OPENFOAM)	δKQ%
0.4	0.3548	0.3775	-6.38%
0.5	0.3068	0.3284	-7.06%
0.6	0.2550	0.2745	-7.67%
0.65	0.2277	0.2458	-7.96%
0.7	0.1995	0.2167	-8.60%
0.8	0.1406	0.1541	-9.59%
0.9	0.0786	0.0824	-4.91%

Table 5.12 KQ Comparison with B-SERIES Data

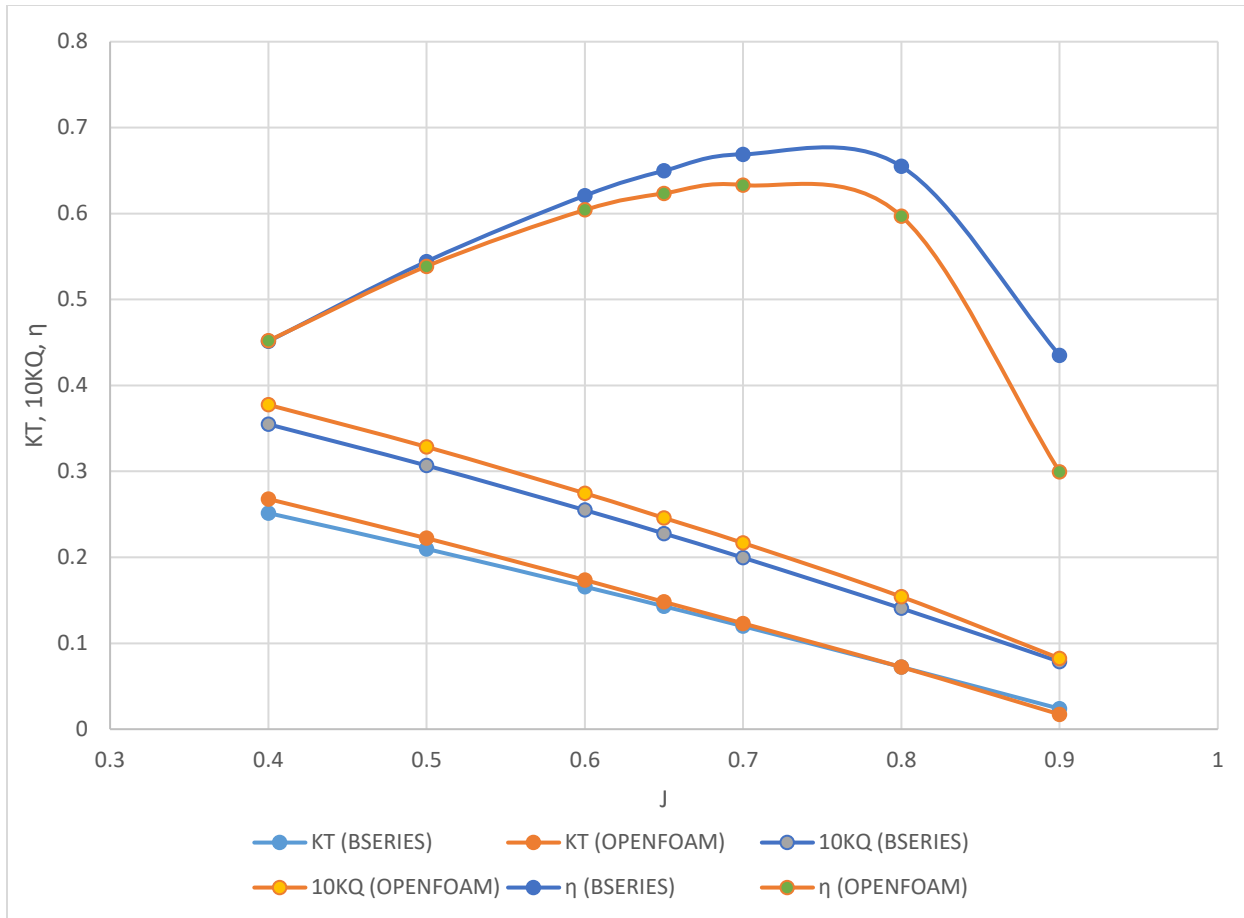| J	η (B-SERIES)	η (OPENFOAM)	Δη%
0.4	0.4512	0.4519	-0.17%
0.5	0.5442	0.5386	1.02%
0.6	0.6209	0.6042	2.68%
0.65	0.6497	0.6235	4.04%
0.7	0.6690	0.6332	5.34%
0.8	0.6549	0.5970	8.85%
0.9	0.4350	0.2995	31.15%

Table 5.13 η Comparison with B-SERIES Data

Figure 5.18 OpenFOAM - B SERIES Open Water Curves Comparison

Firstly, important to note is that for the propeller studied, the values calculated for J=0.9 are out of engineering interest, see e.g., Ntouras et al, (2022). There is a maximum percentage difference of 6.5% for KT, 9.59% for KQ, and a maximum of 8.85% for open water efficiency in the J=0.4–0.8 region. The torque coefficient appears to be overpredicted by the CFD calculations, but the KT prediction is fairly accurate. In the current study as well as in other similar computational studies, the overprediction of KQ appears to be a common tendency, see e.g., Papakonstantinou (2019) and Kalatzis (2020).

The reasons for the value deviations are most probably the following:

1. **Geometry Deviation:** As stated in subsection 5.2.2 CAD Model Generation, the geometry of the generated propeller is close to the B-Series definitions but can deviate to some extent.

2. **Weakness of the Boundary Layer Mesh:** As explained in subsection 5.4.5 Mesh Generation, more layers with thinner size should be placed on the mesh near the propeller wall, in order to predict the boundary layer velocity profile accurately.
3. **Lack of Transition Model:** As it is experimentally verified by Funeno (2002), a transition from laminar to turbulent flow takes place on the blade surface. The k-Ω SST turbulence model describes the laminar and turbulent regions accurately but lacks capability to describe the region of transition. A transition SST model application as practiced by Kalatzis (2020), could improve the results.
4. **MRF Approximation:** Inducing the propeller rotation through the non-absolutely accurate MRF method, reduced the accuracy of the predictions.
5. **Duration of the Simulation:** Had more computational hours been available, more iterations would have improved convergence.

This comparison with the B-Series Data is conducted for the cause of validating the CFD procedure as required according to AIACS Recommendation No. 173 (November 2022) - Guidelines on Numerical Calculations for the purpose of deriving the Vref in the framework of the EEXI Regulation. In the relevant propeller operating range, the discrepancies between the numerical and expected results should not exceed 3% (comparison on the basis KT, 10KQ, and η). The advance coefficient in which the propeller is anticipated to function when mounted on the vessel and for the EEXI condition of relevance for the analysis is known as the relevant operating range.

Therefore, as relevant operating range, the range of advance coefficients where the maximum efficiency is achieved is considered: J=0.6-0.8.

The relative difference of the thrust coefficient values is acceptable at J=0.7 and J=0.8 while at J=0.6 and J=0.65 the relative difference is very close to the AIACS acceptable limit (3%).

The relative difference values of the torque coefficient (KQ) have a considerable value which indicates overprediction of KQ, that is also observed in similar studies as explained earlier. These values deviate from the AIACS acceptable limit (3%).

The relative difference of the efficiency (η) values is acceptable at J=0.6 while it is very close to the acceptable limit (3%) at J=0.65 and J=0.7. At J=0.8 there is a small deviation.

5.8 Comparison with Experimental and MaPFlow data

J	KT (EFD)	KT (OPENFOAM)	δKT%
0.4	0.2509	0.2678	-6.72%
0.5	0.2092	0.2222	-6.21%
0.6	0.1642	0.1736	-5.71%
0.65	0.1409	0.1481	-5.07%
0.7	0.1182	0.1231	-4.16%
0.8	0.0688	0.0722	-4.92%
0.9	0.0168	0.0172	-2.50%

Table 5.14 KT Comparison with EFD

J	10KQ (EFD)	10KQ (OPENFOAM)	δKQ%
0.4	0.3534	0.3775	-6.81%
0.5	0.3062	0.3284	-7.25%
0.6	0.2537	0.2745	-8.22%
0.65	0.2255	0.2458	-9.01%
0.7	0.1973	0.2167	-9.81%
0.8	0.1398	0.1541	-10.22%
0.9	0.0786	0.0824	-4.86%

Table 5.15 KQ Comparison with EFD

J	η (EFD)	η (OPENFOAM)	δη%
0.4	0.4504	0.4519	-0.34%
0.5	0.5425	0.5386	0.72%
0.6	0.6163	0.6042	1.96%
0.65	0.6434	0.6235	3.08%
0.7	0.6580	0.6332	3.77%
0.8	0.6206	0.5970	3.81%
0.9	0.3220	0.2995	6.97%

Table 5.16 Efficiency (η) Comparison with EFD

Comparing the results with the EFD values, within the relative operating range (J=0.6-0.8), they are satisfactory, especially the thrust coefficient and the efficiency where the relative difference has a maximum value of 5.71% and 3.81% respectively. At J=0.6 and J=0.65 the efficiency relative difference is accepted by AIACS. The other efficiency values are remarkably close to the limit (3%).
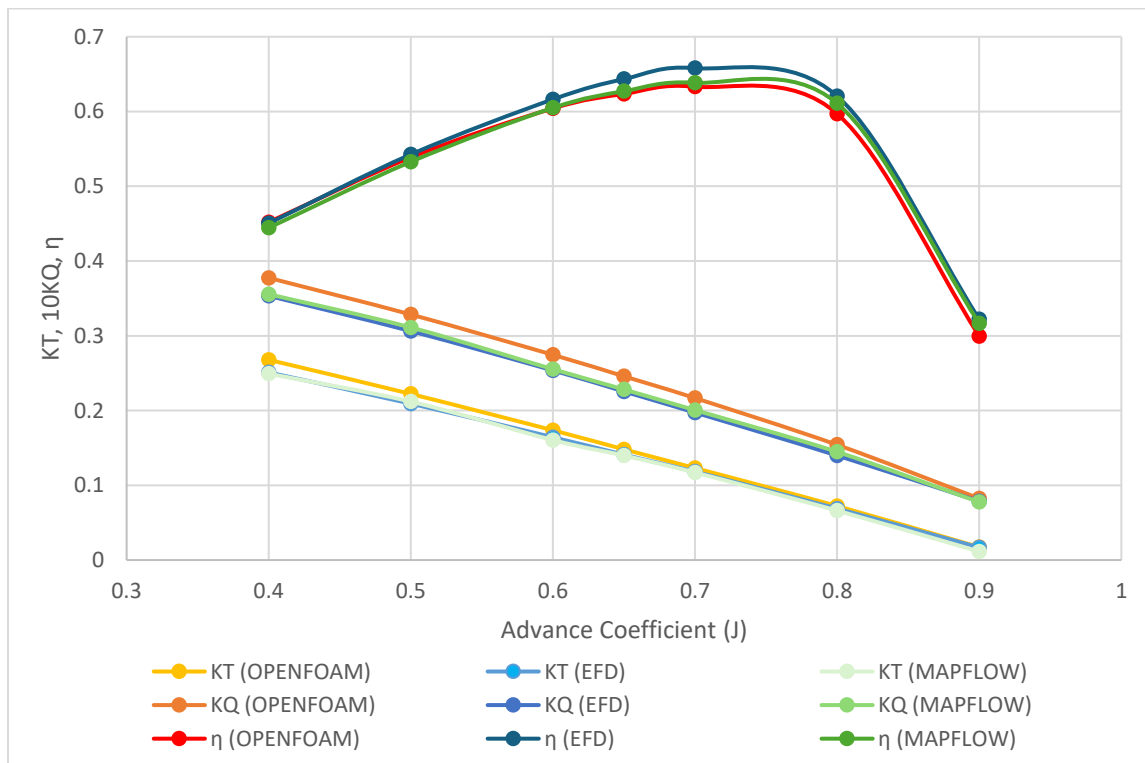

Figure 5.19 OpenFOAM - EFD - MaPFlow Comparison

As seen in figure 5.15 above, the results of the study of Ntouras et al, called **MARTECH**, (2022) where the inhouse solver MaPFlow was used, have better agreement in comparison with the ones of this study (OpenFOAM). The reasons are most probably the following:

1. **Geometry Accuracy:** The CAD model used in Martech study is derived by scanning the original model used in towing tank experiments, by an industrial scanner (FAROS), to guarantee that exactly the same geometry is used for the CFD simulation. Therefore, there were no geometry deviations. Furthermore, as seen in figure 5.16 where the two propellers (the one used for this study has the metallic color, and the one used for the Martech study, has the white color), the difference is considerable:
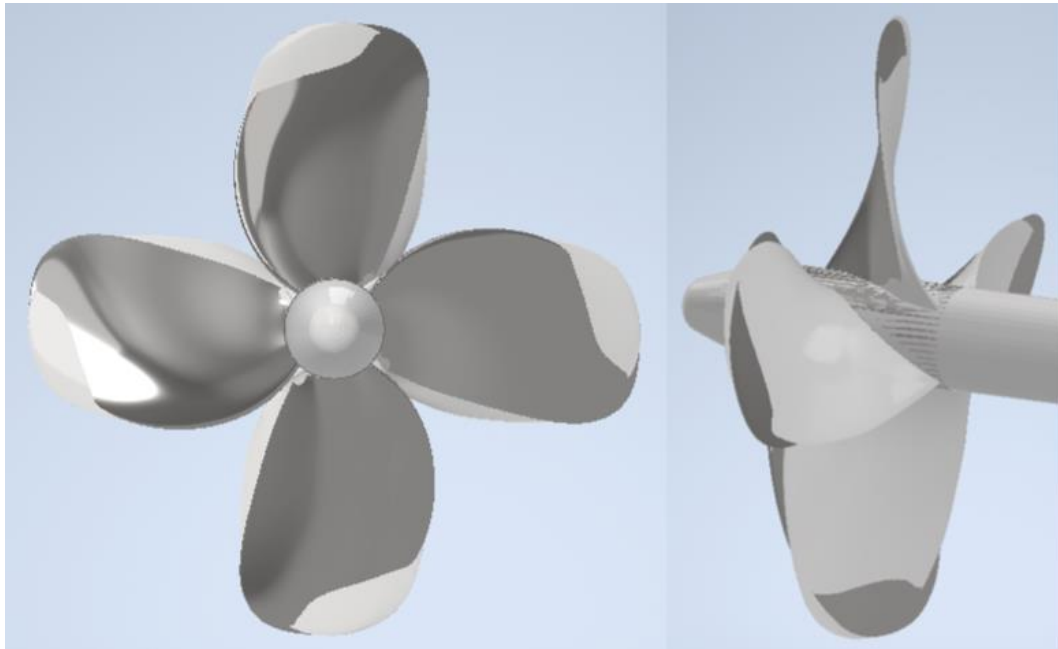

Figure 5.20 Comparison Between the Two Geometries

2. **Propeller Rotation Method:** To induce the rotation of the propeller, the solution of the governing equations in Martech study was conducted in the relative reference frame, which rotates the propeller body itself

providing accuracy, and not the MRF approximation which is the only option to induce rotation in Simscale for steady state simulations.

3. **Layer Management:** A greater number of thinner layers (about 20) was used in Martech study for the purpose of accurately capturing the boundary layer information. In the case of this study, this practice would be not feasible due to the limited computational resources.

4. **Mesh Generation Process:** The mesh used in Martech study was generated through a software that allows manual handling, and by that way a freedom of refinement movements was allowed, while the unnecessary refinements were avoided.

5.9 Visualization

Before presenting the following figures, it must be noted that for the cause of better visualization, the color scale is rescaled to custom data range different for each case.
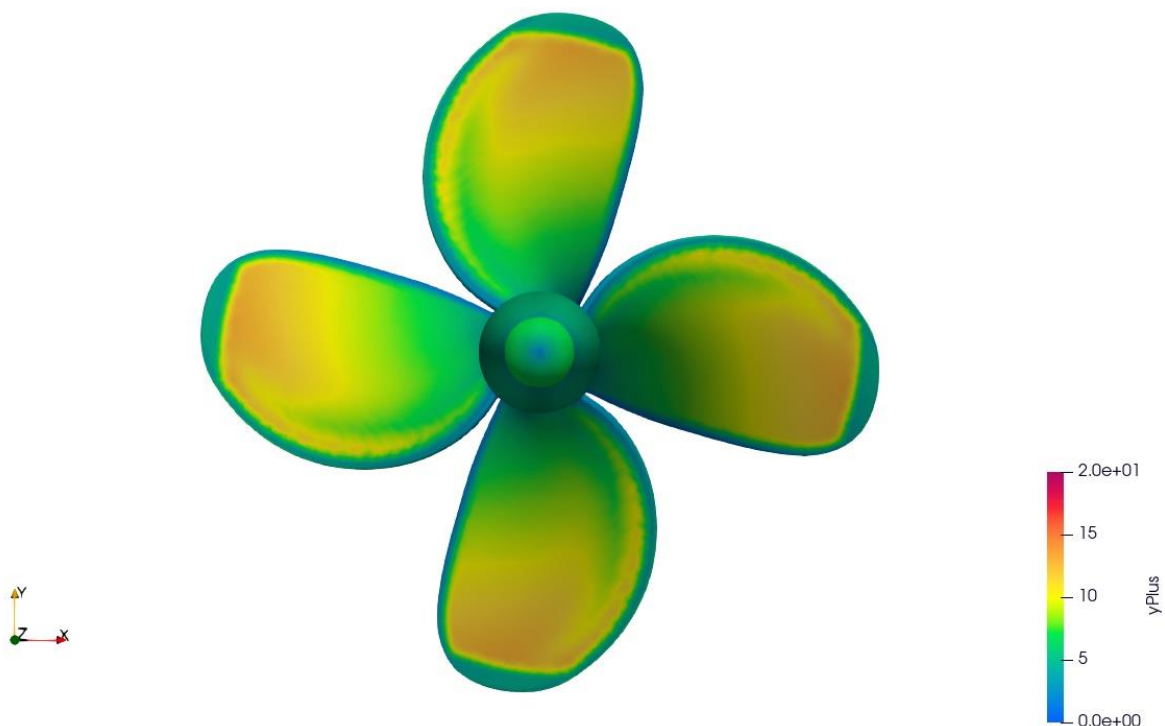

Figure 5.21 Y+ Values Distribution Along the Propeller Surface

As seen in figure 5.17, the achieved y+ values are less than 7 at the propeller tips, leading and trailing edges, and the hub, and less than 15 at the rest of the blade surface.
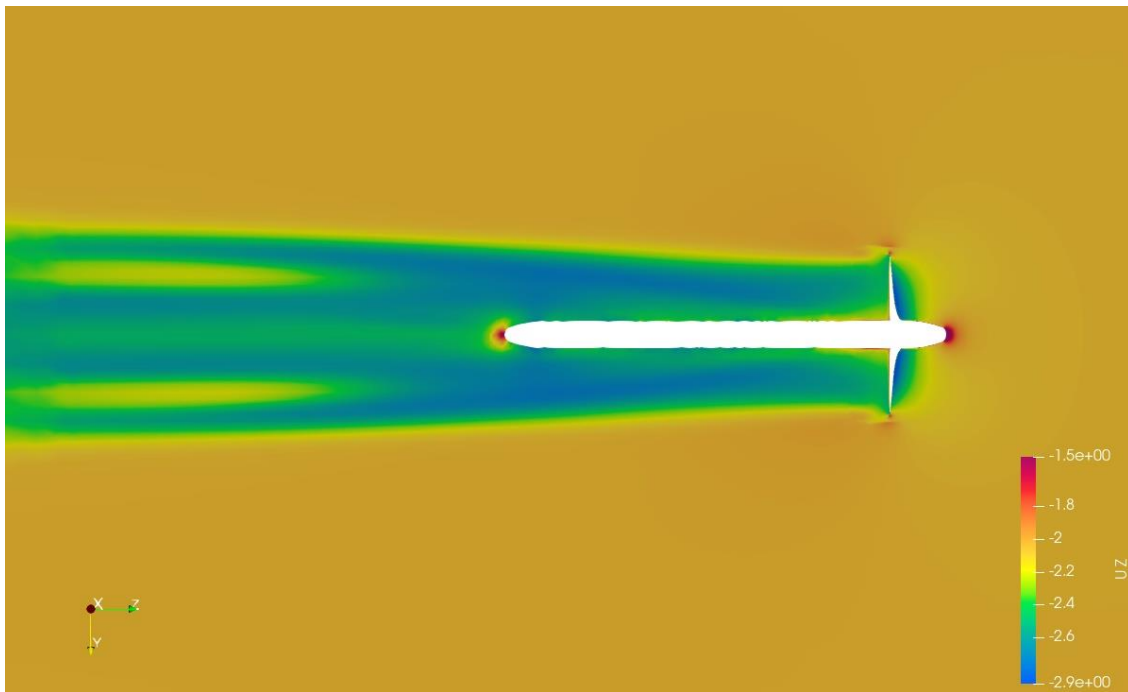

Figure 5.22 Axial Velocity at J=0.7 – Longitudinal View

In figure 5.18 one can observe the rise of velocity values (acceleration) downstream which is responsible for the thrust force acting upstream and moving the vessel forward. There is also a stagnation point at the point of the upstream hub where the velocity is zero. At the end of the downstream hub flow, separation can be noticed where recirculation takes place.
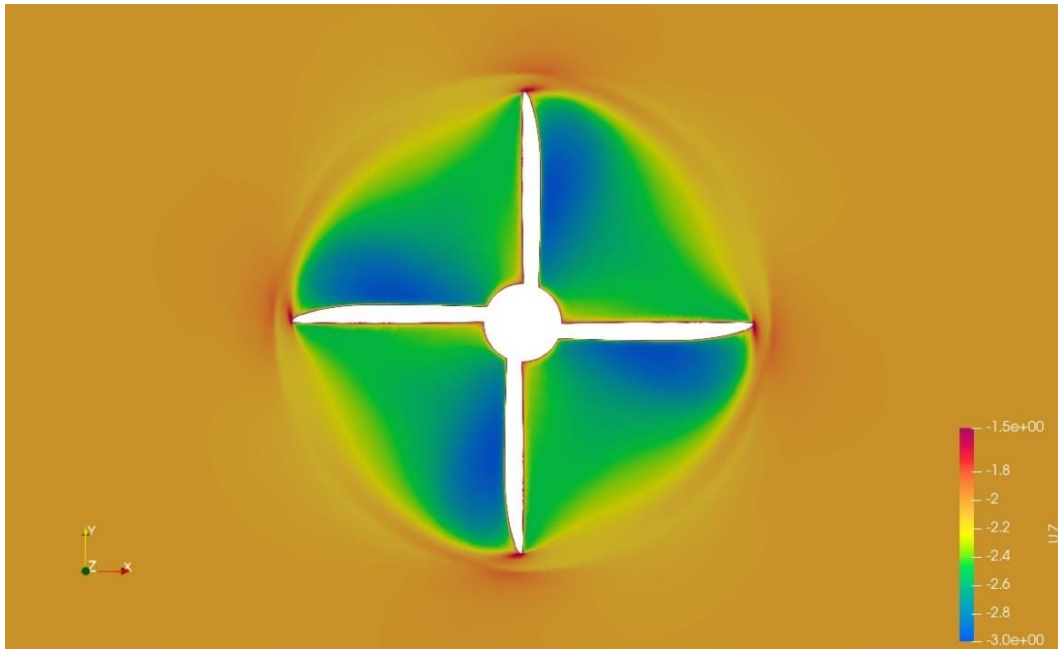
Figure 5.23 Axial Velocity at J=0.7 - Sectional View (z=0)

In figure 5.19 a sectional slice at z=0 can be seen. For the purpose of simplifying the visualization of the sectional views in figures 5.19 and 5.21, the plane used for slicing, is shown in figure 5.20 below:
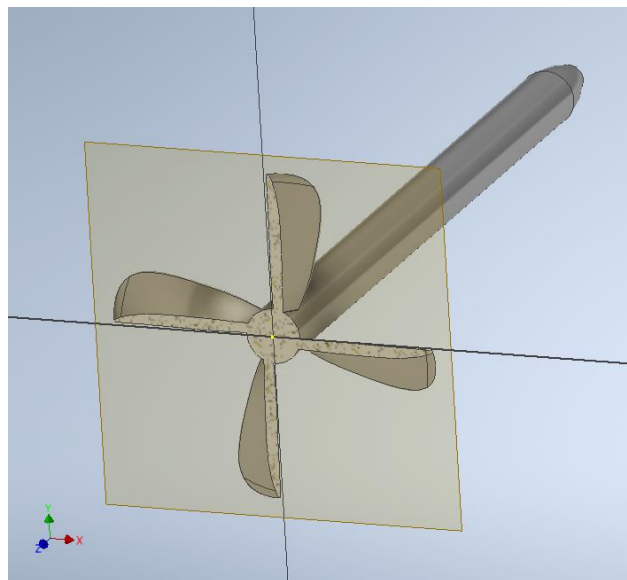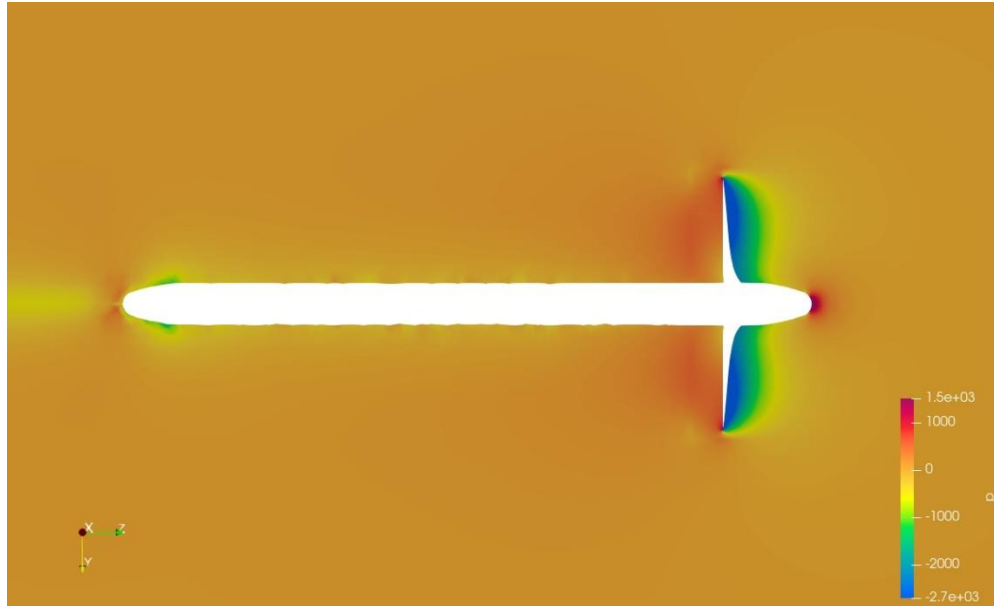

Figure 5.24 Sectional Plane at z=0

Figure 5.25 Pressure Distribution at J=0.7 - Longitudinal View

In figure 5.21, as expected, the positive pressure values at the left side (downstream pressure side) of the blades and the negative at the right (upstream suction side). This pressure difference between the two sides of the blades causes acceleration of the water downstream as seen in figure 5.15, satisfying Bernoulli's principle. While the water is accelerated downstream, it generates thrust which is a force acting in the upstream direction as the law of momentum conservation describes and is responsible for the vessels' forward movement.
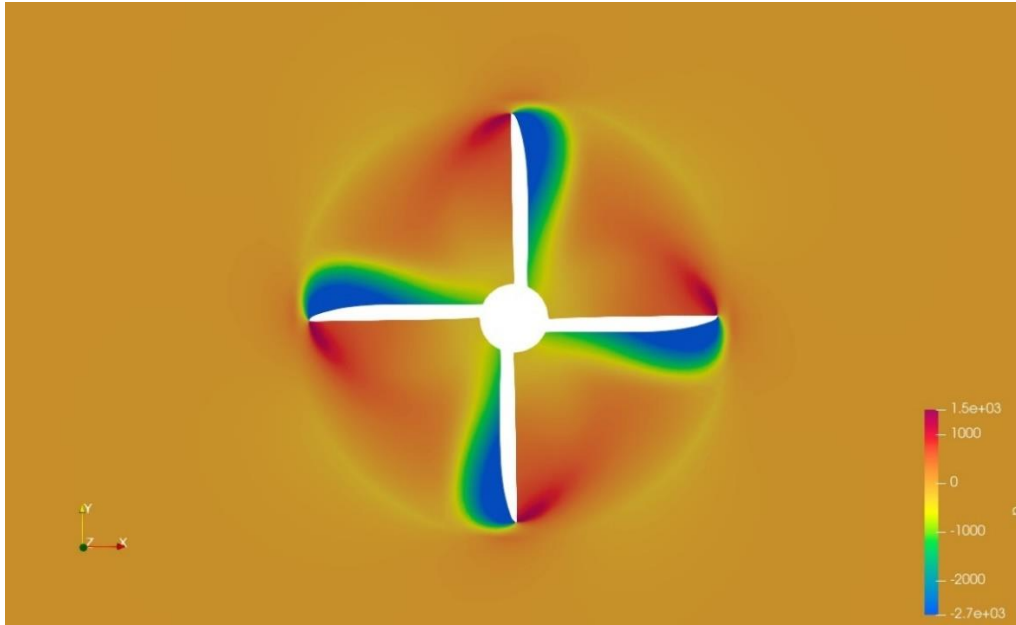
Figure 5.26 Pressure Distribution at J=0.7 - Sectional View

In figure 5.22 a sectional clip view at z=0 can be seen.

For the visualization of the vortical structures around the blade, the Q criterion is used. In 3 dimensions the gradient of the velocity is a second-order tensor which can be expressed as the matrix **L**:

$$L = \nabla U = \begin{bmatrix} \dfrac{\partial u_x}{\partial x} & \dfrac{\partial u_y}{\partial x} & \dfrac{\partial u_z}{\partial x} \\ \dfrac{\partial u_x}{\partial y} & \dfrac{\partial u_y}{\partial y} & \dfrac{\partial u_z}{\partial y} \\ \dfrac{\partial u_x}{\partial z} & \dfrac{\partial u_y}{\partial z} & \dfrac{\partial u_z}{\partial x} \end{bmatrix}$$

L can be decomposed as:

$$L = \frac{1}{2}(L + L^T) + \frac{1}{2}(L - L^T)$$

Where, the symmetric part denoted as S is the strain rate tensor:

$$S = \frac{1}{2}(L + L^T)$$

71

And the antisymmetric part denoted as Ω is the rotation rate or vorticity (spin) tensor:

$$\Omega = \frac{1}{2}(L - L^T)$$

A spatial region is defined by the Q criterion, where:

$$Q = \frac{1}{2}[\|\Omega\|^2 - \|S\|^2] > 0 \qquad\qquad (5.1)$$

Therefore, Q represents the local balance between shear strain and vorticity magnitude. The Iso–surfaces of Q are illustrated in figures 5.23 and 5.24 below, colored with axial velocity – z. Fine mesh is required to capture the vortices, see e.g., Papakonstantinou (2019). Thus, they stop where the MRF Zone refinement ends downstream (figures 5.10 and 5.24).
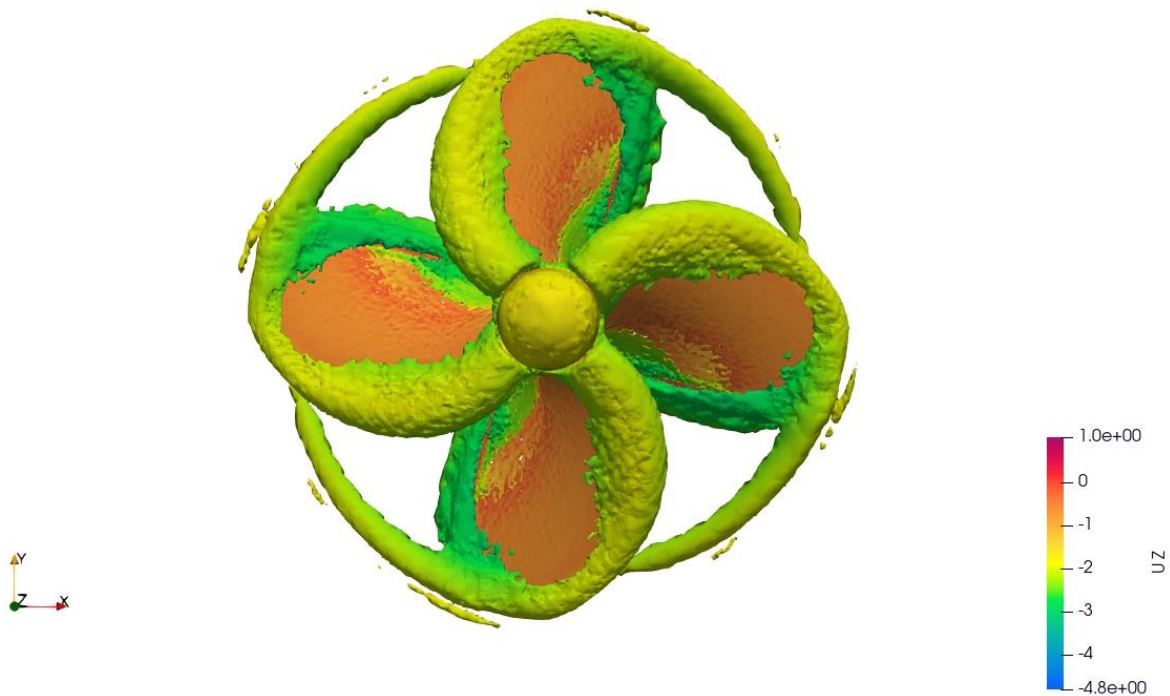

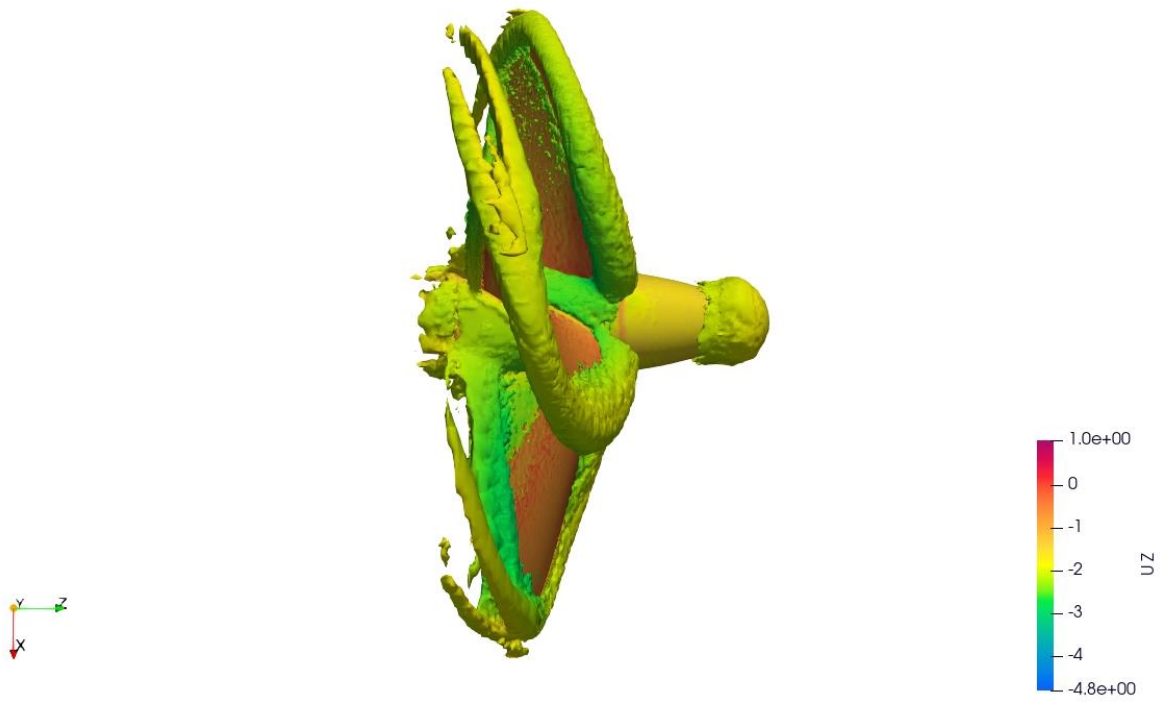*Figure 5.27 Tip Vortex Visualization at J=0.7 – Sectional View*

Figure 5.28 Tip Vortex Visualization at J=0.7 – Longitudinal View

6 Conclusions and Future Work

To summarize, the current study's objective was to determine the open water characteristics through the cloud-based platform of SimScale which used the open-source simulation code OpenFOAM. About 5.6 million cells are necessary to accomplish mesh independence. Bibliographic and experimental data, as well as a visualization of the velocity and pressure field, are used for validation. A maximum deviation of 6.5% is observed for KT, 9.59% for KQ and 8.85% for efficiency from the official bibliographic data. The deviations occurred mainly because of the geometry discrepancies, the boundary layer mesh weakness, the MRF zone approximation and the weakness of the turbulence model k-Ω SST to describe the region of flow transition from laminar to turbulent. The majority of the taken decisions and the settings chosen in the present thesis project had to do with the computational cost. Consequently, given that additional computational resources and more software options such as rotation with relevant frame of reference and transition turbulence model are available, the results could be improved in a future study.

Furthermore, as a future work, a ship self-propulsion simulation i.e. the calculation of the flow around the hull that advances at uniform speed due to the action of its own propeller, could be conducted. Ship self-propulsion performance prediction is one of the most important factors for the energy-efficient design of a ship and represents one of the most interesting engineering problems.

Another future work could be the study of the effects of propeller energy saving devices (ESDs) through CFD simulations. ESDs are systems designed to improve the efficiency of the ship propulsion. Many kinds of ESDs have been developed, which can be retrofitted to existing vessels or installed in new buildings. ESDs may include a range of devices, such as pre-ducts that can achieve 2-6% propulsion efficiency improvements, pre-swirl fins (4-8% efficiency improvement), hub caps with fins (0.5-2% efficiency improvement), and twisted rudders and bulbs (1.5-5% efficiency improvement).

7 References

ABS (2021), Practical Considerations for Underwater Noise Control

Anderson, P. (1997) A Comparative study of conventional and tip-fin propeller performance. In Twenty-First Symposium on Naval Hydrodynamics; The National Academy Press: Washington, DC, USA

Anevlavi, D., Zafeiris, S., Papadakis, G., & Belibassakis, K. (2023). Efficiency Enhancement of Marine Propellers via Reformation of Blade Tip-Rake Distribution. Journal of Marine Science and Engineering, 11(11), 2179

ANSYS, Inc. ANSYS FLUENT 12.0 - Theory guide, 2009

AQUO (2015). Report R2.9, Ship Underwater Radiated Noise Patterns, Achieve Quieter Oceans by shipping noise footprint reduction (FP7 Project No314227)

Bacalja Bašić, B., Krčum, M., & Jurić, Z. (2024). Propeller optimization in marine power systems: Exploring its contribution and correlation with renewable energy solutions. *Journal of Marine Science and Engineering*, *12*(5), 843

Belibasakis, K. A., & Politis, G. K. (1998). A nonlinear velocity based boundary element method for the analysis of marine propellers in unsteady flow

Belibassakis, K., & Politis, G. (2019). Generation and propagation of noise from cavitating marine propellers. In Symposium on Marine Propulsors smp: Rome, Italy

Bernitsas, M. M., Ray, D., & Kinley, P. (1981). *KT, KQ and efficiency curves for the Wageningen B-series propellers*, University of Michigan

Bilgili, L., & Ölçer, A. I. (2024). IMO 2023 strategy-Where are we and what's next?. *Marine Policy*, *160*, 105953

Brizzolara, S., Villa, D., & Gaggero, S. (2008, September). A systematic comparison between RANS and panel methods for propeller analysis. In *Proc. Of 8th International Conference on Hydrodynamics, Nantes, France*

Carlton, J. (2018). *Marine propellers and propulsion*. Butterworth-Heineman

Chiroșcă, A. M., & Rusu, L. (2021). Comparison between model test and three CFD studies for a benchmark container ship. *Journal of Marine Science and Engineering*, *9*(1), 62

Dalheim, Ø. Ø. (2015). *Development of a Simulation Model for Propeller Performance* (Master's thesis, NTNU).

Diffenbaugh, N. S., & Barnes, E. A. (2023). Data-driven predictions of the time remaining until critical global warming thresholds are reached. *Proceedings of the National Academy of Sciences*, *120*(6), e2207183120

Faber, J., Hanayama, S., Zhang, S., Pereda, P., Comer, B., Hauerhof, E., ... & Xing, H. (2020). Fourth IMO GHG Study. *London, UK*

Fine, N. E., & Kinnas, S. A. (1993). A boundary element method for the analysis of the flow around 3-D cavitating hydrofoils. *Journal of ship research*, *37*(03), 213-224

Fluid Mechanics 101 (2019): [CFD] The k – omega SST Turbulence Model, https://www.youtube.com/watch?v=myv-ityFnS4&t=679s&pp=ygVGRmx1aWQgTWVjaGFuaWNzIDEwMSAoMjAxOSk6IFtDRkRdIFRoZSBrIOKAkyBvbWVnYSBTU1QgVHVyYnVsZW5jZSBNb2RlbA%3D%3D

Fluid Mechanics 101 (2020): [CFD] The k-omega Turbulence Model, https://www.youtube.com/watch?v=26QaCK6wDp8&t=902s&pp=ygU-Rmx1aWQgTWVjaGFuaWNzIDEwMSAoMjAyMCk6IFtDRkRdIFRoZSBrLW9tZWdhIFR1cmJ1bGVuY2UgTW9kZWw%3D

Fluid Mechanics 101 (2021): [CFD] Eddy Viscosity Models for RANS and LES, https://www.youtube.com/watch?v=SVYXNICeNWA&pp=ygVIRmx1aWQgTWVjaGFuaWNzIDEwMSAoMjAyMSk6IFtDRkRdIEVkZHkgVmlzY29zaXR5IE1vZGVscyBmb3IgUkFOUyBhbmQgTEVT

Froude, R.E. (188). On the part played in the operation of propulsion differences in fluid pressure. Trans. RINA, 30

Funeno, I. (2002), On Viscous Flow around Marine Propellers. Journal of the Kansai Society of Naval Architects 2002, 238

Greeley, D. S. (1982). Numerical method for propeller design and analysis in steady flow. *SNAME Transaction*, *90*, 415-453

Hanson, L., Jawahar, H. K., Vemuri, S. S., & Azarpeyvand, M. (2023). Experimental investigation of propeller noise in ground effect. Journal of Sound and Vibration, 559, 117751

Holzmann T. (2017), Mathematics Numerics, Derivations and OpenFOAM, Leoben, 2017

IMO (2014). Guidelines for the Reduction of Underwater Noise from Commercial Shipping to Address Adverse Impacts on Marine Life – non mandatory technical advices, International Maritime Organization MEPC.1/Circ.833

IMO (2018), Adoption of the Initial IMO Strategy on Reduction of GHG Emissions from Ships and Existing IMO Activity Related to Reducing GHG Emissions in the Shipping Sector, 2018.Initial IMO GHG Strategy (2018)

IMO (2023) Strategy on Reduction of GHG Emissions from Ships

ITTC 7.5-03-01-04 - Recommended Procedures and Guidelines (1999), *CFD, General CFD Verification*

ITTC 7.5-03-03-01 - Recommended Procedures and Guidelines (2014), *Practical Guidelines for Ship Self-Propulsion CFD*

Jasak H. (1996), Error analysis and estimation for the finite volume method with application to fluid flows, London: PhD Thesis, Imperial College of Science, Technology and Medicine, 1996

Kalantzis K.N. (2020). Numerical simulation of propeller open water characteristics using CFD

Kerwin, J. E., & Lee, C. S. (1978). *Prediction of steady and unsteady marine propeller performance by numerical lifting-surface theory* (No. Paper No. 8)

Kinnas, S. A. (1996). Theory and numerical methods for the hydrodynamic analysis of marine propulsors. *Advances in marine hydrodynamics*, *5*, 279-322

Krasilnikov, V. (2019). CFD modelling of hydroacoustic performance of marine propellers: Predicting propeller cavitation. In Proceedings of the 22nd Numerical Towing Tank Symposium, Tomar, Portugal (Vol. 29)

Lafeber, F. H., Bosschers, J., Hämäläinen, R., & Lönnberg, B. (2013). Underwater radiated noise measurements for a cruise ferry. *Proceedings of the PRADS2013*, *20*, 25

Lerbs, H. W. (1951). On the effects of scale and roughness on free running propellers. *Journal of the American Society for Naval Engineers*, *63*(1), 58-94

Lidtke, A. K., Lloyd, T., Lafeber, F. H., & Bosschers, J. (2022). Predicting cavitating propeller noise in off-design conditions using scale-resolving CFD simulations. *Ocean Engineering*, *254*, 111176

Lloyd, T., Foeth, E., Lafeber, F. H., & Bosschers, J. (2020). Progress in the prediction and mitigation of propeller cavitation noise and vibrations. In *Proc. of 26th International Virtual HISWA Symposium*

Louisiana State University (LSU). (n.d.). CFD Simulations, WISE ResearchModel Tests, Wartsila Encyclopedia of Marine and Energy Technology

Mehdipour, R. (2014). Simulating propeller and propeller-hull interaction in openfoam

Michigan Wheel (2000), *Propeller Geometry: Terms and Definitions*

Njaastad, E.B., Steen, S. & Egeland, O. (2022) Identification of the geometric design parameters of propeller blades from 3D scanning. *J Mar Sci Technol* 27, 887–906

Ntouras, D., Papadakis, G., Liarokapis, D., Trachanas, G., & Tzabiras, G. (2022). Numerical and experimental investigation of a model scaled propeller. *Trends in Maritime Technology and Engineering*, 409-415

Oosterveld, M. W. C., & van Oossanen, P. (1975). Further computer-analyzed data of the Wageningen B-screw series. *International shipbuilding progress*, *22*(251), 251-262

Papadakis, G. (2014). Development of a hybrid compressible vortex particle method and application to external problems including helicopter flows. National Technical University of Athens

Papakonstantinou, T., Grigoropoulos, G., & Papadakis, G. (2019). Marine propeller optimization using open-source CFD. In *Sustainable Development and Innovations in Marine Technologies* (pp. 252-259). CRC Press

Patankar, S. V. (1980), Numerical Heat Transfer and Fluid Flow, Taylor and Francis.

Patankar, S. V. & Spalding, D. B. (1972). A calculation procedure for heat, mass and momentum transfer in three-dimensional parabolic flows. International Journal of Heat and Mass Transfer, 15(10), 1787–1806.

Politis, G. (2015), Hydrodynamics of Mordern Propulsion Systems

Politis, G. (2019), Ship Resistance and Propulsion

Polyzos S., Calculation of the Hydrodynamic Resistance of Appendages on Conventional Vessels, Athens, 2017

Regan Nelson (2023), Why All the Concern About Ship Noise? NRDC

Salvatore, F., Streckwall, H., & Van Terwisga, T. (2009, June). Propeller cavitation modelling by CFD-results from the VIRTUE 2008 Rome workshop. In Proceedings of the first international symposium on marine propulsors, Trondheim, Norway (pp. 22-24)

Simscale (2024), Rotating Zones

Troost, L. (1940) Open water test series with modern propeller forms.

UN, Paris Agreement, Paris, 2015

Underwater Noise, Protecting the Maritime Environment, EMSA

Windgrove (2014), CFD analysis could replace model testing